Volume 17

LLE Review

Quarterly Report

October–December 1983

Laboratory for Laser Energetics
College of Engineering and Applied Science
University of Rochester
250 East River Road
Rochester, New York 14623

Volume 17

LLE Review

Quarterly Report

Editor: R. Epstein
(716) 275-5405

October–December 1983

Laboratory for Laser Energetics
College of Engineering and Applied Science
University of Rochester
250 East River Road
Rochester, New York 14623

IN BRIEF

This volume of LLE Review features articles on the infrared-to-ultraviolet conversion of six beams of OMEGA and on the first series of experiments conducted with the reconfigured, up-converted system; developments in the LLE advanced technology program; and activity in the National Laser Users Facility.

The OMEGA conversion and the initial six-beam experiments have been conducted to meet the system performance criteria established by the Department of Energy as the basis for a decision for the continued up-conversion of the system. The specific criteria and the experimental data to be obtained are listed below.

Laser System Performance Criteria: (a) energy in the six converted (351-nm) beams greater than 250 J in a pulse greater than 0.5 ns; (b) ultraviolet conversion efficiency in reasonable agreement with theoretical predictions; (c) measurement and successful evaluation of the beam-intensity distribution in the equivalent target plane in the ultraviolet (351 nm) and in the infrared (1054 nm); (d) alignment accuracy (pointing, focusing, and stability) of the six ultraviolet beams comparable to the infrared beam capability.

Target Interaction Experiments with Six-Beam Ultraviolet Illumination: (a) measurement of absorption on spherical targets consistent with theoretical predictions; (b) measurement of preheat as indicated by the x-ray spectrum from an illuminated spherical target. these measurements should be in reasonable agreement with data from

one-beam planar target experiments and should show lower preheat levels than similar infrared experiments; (c) measurement of the mass-ablation rate for spherical targets and demonstration that this rate is comparable to or greater than the rate observed in similar infrared experiments.

The Laboratory for Laser Energetics completed the six-beam OMEGA conversion (LLE Review, Volume 16) and has performed the experiments specified in the decision criteria. This volume describes how the required criteria were met or surpassed.

In particular, in the OMEGA Facility Report: (a) System 351-nm performance at the level of 388 J was demonstrated. A series of 103 shots was taken; 30 of these shots produced energy in excess of 250 J. (b) The frequency-conversion performance was in reasonable agreement with the *MIXER* code (LLE Review, Volume 16). (c) Both the 351-nm and 1054-nm equivalent-target-plane distributions were measured and evaluated. (d) Pointing stability of $\pm 10\,\mu$m and focus resolution of $\pm 50\,\mu$m at 351 nm, comparable to 1054-nm performance, was demonstrated.

The Progress in Laser Fusion section describes the experimental work that demonstrated: (a) Absorption at 10^{15} W/cm^2 in excess of 50% was measured, exceeding initial expectations. (b) Preheat levels deduced from x-ray spectra are much less than in comparable 1054-nm experiments. (c) Ablation rates are higher than those measured in comparable 1054-nm experiments.

Following a review, the Department of Energy has granted approval for the conversion of the remaining beams. With the resources currently in hand, a minimum of six additional beams will be converted in FY84. The full conversion of the system is well within our present technical capability.

CONTENTS

Page

IN BRIEF iii

CONTENTS v

Section 1 LASER SYSTEM REPORT 1
- 1.A GDL Facility Report 1
- 1.B OMEGA Facility Report 2
- 1.C OMEGA Wavelength Conversion 3

Section 2 PROGRESS IN LASER FUSION 11
- 2.A Absorption and Hot-Electron Generation Measurements with Spherically Illuminated Targets at λ=351 nm 11
- 2.B Parametric Instabilities in Underdense Spherical Plasmas with λ=351 nm Illumination 18
- 2.C Thermal Transport and Preheat Measurements with Spherically Illuminated Targets at λ=351 nm 32

Section 3 ADVANCED TECHNOLOGY DEVELOPMENTS 43
- 3.A Time-Resolved, Laser-Induced Phase Transition in Aluminum 43

Section 4 NATIONAL LASER USERS FACILITY NEWS 49

PUBLICATIONS AND CONFERENCE PRESENTATIONS

Laboratory Engineer Larry Forsley, leader of the Computer Systems Group, is shown digitizing an x-ray photograph of a target plasma with the recently installed image processing system. Digital image processing is applied extensively in the experimental and engineering programs of the laboratory.

Section 1
LASER SYSTEM REPORT

1.A GDL Facility Report

Throughout the first quarter of fiscal year 1984 (October through December 1983), GDL continued operations as a 351-nm interaction facility. Highlights of the quarter include a very successful campaign for the University of Pennsylvania (see the NLUF News) in the x-ray chamber, holographic experiments, characterization of the UV intensity distribution in the equivalent target plane, and a record number of damage test shots.

Through the latter part of the quarter, demand on GDL slackened, due to the demand for GDL experimental personnel in OMEGA experiments and demands on GDL operations personnel for "twenty-fifth beam" and Kuizenga oscillator integration projects (see the OMEGA Facility Report).

A summary of GDL operations follows:

Interaction Target Shots	59	(15%)
X-Ray Target Shots (Includes 39 NLUF shots)	61	(16%)
Damage Test Target Shots	219	(56%)
Pointing Shots	47	(12%)
Calibration Shots	2	(0.5%)
Miscellaneous Shots	2	(0.5%)
TOTAL	390	(100%)

ACKNOWLEDGMENT

This work was supported by the U.S. Department of Energy Office of Inertial Fusion under contract number DE-AC08-80DP40124 and by the Laser Fusion Feasibility Project at the Laboratory for Laser Energetics which has the following sponsors: Empire State Electric Energy Research Corporation, General Electric Company, New York State Energy Research and Development Authority, Northeast Utilities Service Company, The Standard Oil Company, and University of Rochester. Such support does not imply endorsement of the content by any of the above parties.

1.B OMEGA Facility Report

OMEGA systems operations during this quarter have consisted of acquiring all the necessary data for the successful performance review by DOE on 3 November, continuing to characterize the UV system performance, completing successful target shots for internal and NLUF experimental campaigns, and, finally, completing a series of shots aimed at optically cross-calibrating our 8" Scientech calorimeters.

As the quarter began, we had completed a series of shots for preliminary data to be sent to DOE as a preview of our ability to meet the six-beam UV performance criteria. At the completion of this series, the system was shut down for substantial oscillator repairs, driver alignment, and crystal re-tuning. The shutdown took about two weeks and resulted in a higher, more reliable output power from the oscillator; a better-characterized, stable wavelength; and a better-aligned driver line, which led to significantly improved equivalent-target-plane intensity uniformity. By mid-October, we began firing the system for the completion of the DOE acceptance criteria, including characterization of the equivalent target plane; comparison of the UV output with *MIXER*[1] code predictions; characterization of beam transport; and measurements of pointing and centering accuracy, thermal transport, mass-ablation rate, and absorption. Summaries of the results of these measurements are found in articles appearing later in this volume.

As this experimental campaign ended in early November, further laser system characterization continued. In one series of target shots, we verified that no damaging IR radiation is propagated back through the laser system. Consistent measurements of less than 0.2 J propagating back into the driver line, with up to 70 J of UV (40 J of IR) on target, showed that 72-mm Pockels cells are not necessary as isolation devices for the system. The Pockels cells were therefore extracted from the system, resulting in a 10% increase in energy capability in the beams and possibly eliminating some phase problems noted in the equivalent-target-plane photographs.

By mid-November, target shooting resumed on a regular schedule averaging 12 target shots per day. A series of shots for the University of Maryland (NLUF) were completed, yielding novel XUV spectral data to be reported on elsewhere. Shot series were conducted for internal (LLE) programs studying electron thermal transport and coronal physics.

During the final week of operations in December, the 8" Scientech calorimeters were optically cross-calibrated by means of accurate splitting of the laser beams into each of eight different calorimeters and by moving the calorimeters on each shot to eliminate beam-to-beam variations.

A summary of OMEGA system operations follows:

Target Shots (including 25 NLUF)	140	(39%)
Driver-Centering and Calibration Shots	92	(25%)
Crystal Tuning Shots	26	(7%)
Pointing Shots (including equivalent-target-plane characterization)	18	(5%)
Calorimetry Calibration Shots	41	(11%)
Miscellaneous (failures, software shots)	47	(13%)
TOTAL	364	(100%)

Throughout the first quarter of FY84, in addition to system operations, the operations group has been involved in manufacturing-engineering activities related to the upcoming conversion of at least six more OMEGA beams during this fiscal year. Further activities of the operations group include preliminary design work on the "twenty-fifth beam" project, where the GDL beam is to be synchronized with the OMEGA beams and pointed into the OMEGA target chamber as a backlight. Members of the operations group are on the task force for implementation of Kuizenga oscillators and pre-drivers into both GDL and OMEGA and are taking part in the design of various subsystems of the twenty-fifth beam, such as power-conditioning, active mirrors, safety interlock, synchronization, and alignment.

ACKNOWLEDGMENT

This work was supported by the U.S. Department of Energy Office of Inertial Fusion under contract number DE-AC08-80DP40124 and by the Laser Fusion Feasibility Project at the Laboratory for Laser Energetics which has the following sponsors: Empire State Electric Energy Research Corporation, General Electric Company, New York State Energy Research and Development Authority, Northeast Utilities Service Company, The Standard Oil Company and University of Rochester. Such support does not imply endorsement of the content by any of the above parties.

REFERENCES

1. R. S. Craxton, *Opt. Commun.* **34**, 474 (1980).

1.C OMEGA Wavelength Conversion

The conversion of six OMEGA beams to UV operation entailed decisions on issues such as:

(a) location of frequency-conversion cells,

(b) construction and alignment of frequency-conversion cells,

(c) pointing, focusing, and beam timing for UV beams, and

(d) beam-diagnostic systems.

In the subsections that follow, we discuss the resolution of these design issues of OMEGA and present the pertinent performance data that satisfy the DOE laser-system-performance criteria (see the IN BRIEF section). The construction, alignment, and successful performance of the frequency-conversion cells has been discussed previously in LLE Review.[1]

Frequency-Conversion-System Configuration

OMEGA is a 24-beam, Nd:glass laser system whose design and 1054-nm performance is discussed in Ref. 2. The OMEGA geometry (see Fig. 17.1) allows two basic locations for the conversion crystals: (a) at the focus lens and (b) at the output of the last spatial filter (C/LAOR). C refers to the final, 90-mm rod amplifier of the laser system, and LAOR refers to the large-aperture optical retarder used in the 1054-nm operation of the system.

Placing the frequency-conversion crystals near the target chamber presents two advantages over the LAOR option:

(a) high-power UV propagation is limited to less than 1 m, and

(b) the focus lens and blast shield are the only optics subject to possible coating damage due to high UV fluxes.

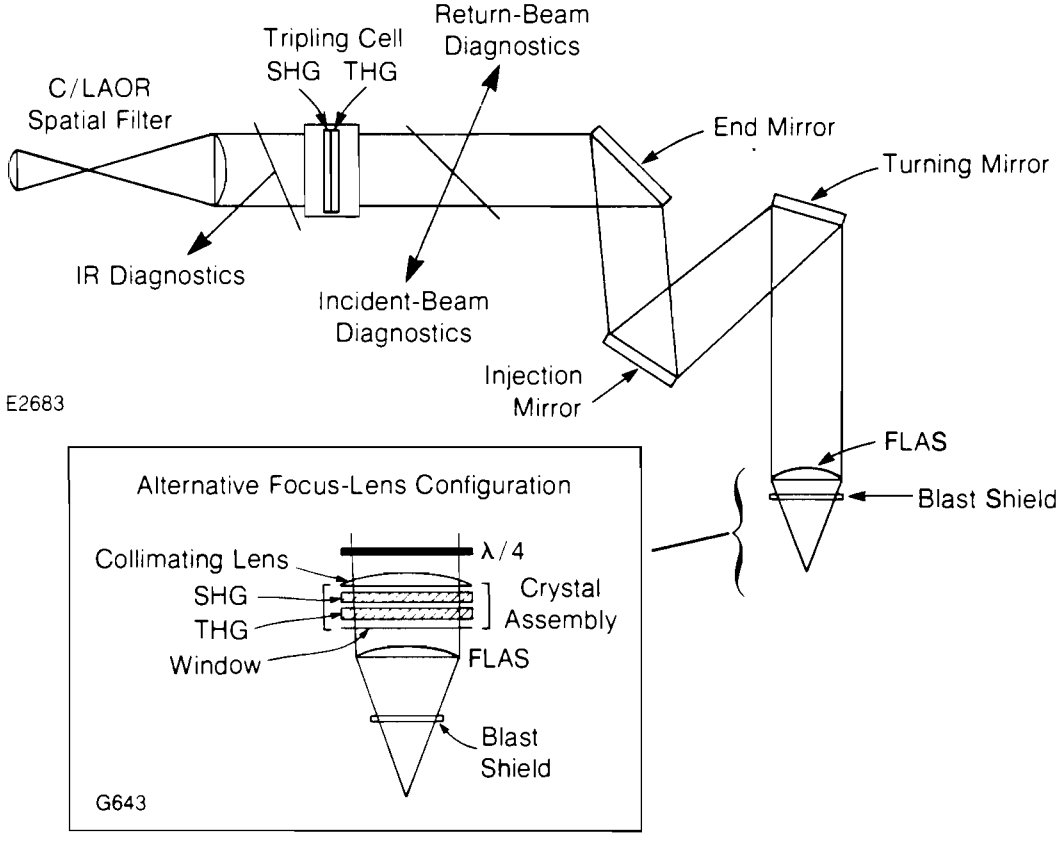

Fig. 17.1
Schematic of the OMEGA 351-nm conversion system. The second-harmonic generator (SHG) and third-harmonic generator (THG) crystals are shown mounted at the output of the last spatial filter (C/LAOR). The rejected alternative location near the focus lenses is indicated in the inset.

Unfortunately, placing the conversion system near the target-focusing lenses also presents some significant disadvantages, compared to the LAOR option, namely:

(a) limited UV-beam diagnostics (the UV diagnostics require retroreflection and a double-pass through the crystals), and

(b) the more complicated opto-mechanical design for such a system which would result in higher cost and longer design/construction time than the LAOR option.

Our favorable long-path-propagation experience with both GDL and OMEGA gave us confidence that UV-beam propagation from the laser bay to the target chamber would not present any serious problems. The primary trade-off between the two design options was between the diagnostic considerations and coating-damage risks.

An estimate of OMEGA flux levels in the UV indicates that at an energy level of 90 J at 351 nm, the highest estimated flux, 1.8 J/cm², occurs at the blast shield. The highest flux at the mirrors at the 90-J

Fig. 17.2
Schematic of the overall beam layout for the OMEGA six-beam UV conversion. The beams shown in dashed lines are 351-nm beams.

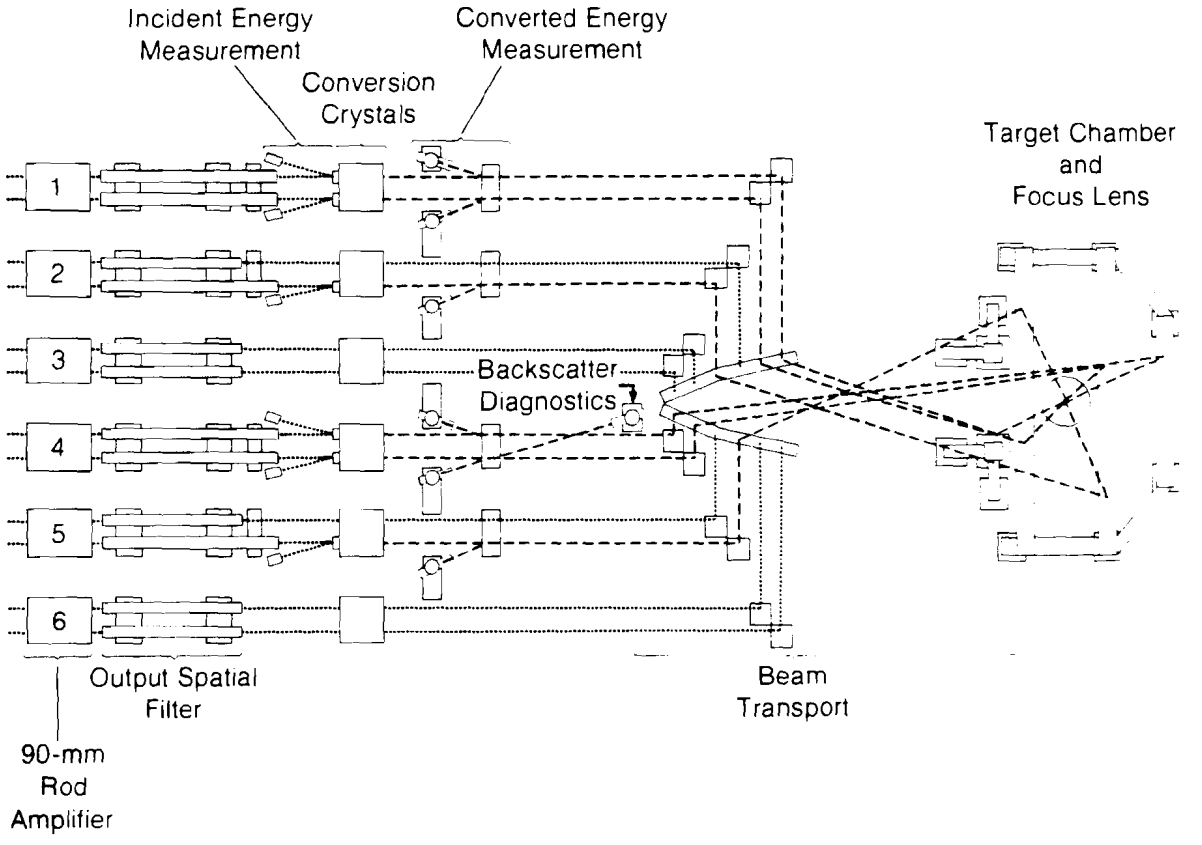

energy level is 1.1 J/cm^2. In these estimates, an average fill factor of 0.6 is assumed. An additional fill-factor multiplier of 0.56 is used to account for local hot spots from beam defects and diffraction rings.

Coating damage measurements at LLE and elsewhere indicate that flux levels of 1.1-1.8 J/cm^2 are below the damage threshold for state-of-the-art 351-nm AR and HR coatings.[3] Results of damage testing conducted at LLE show 1ω-3ω AR/0° coatings with mean damage thresholds ranging from 1.6±0.3 J/cm^2 to 2.1±0.3 J/cm^2. Measurements of 1ω-3ω HR/45° and 57° coatings show damage thresholds ranging from 1.80±0.24 J/cm^2 to 2.6±0.3 J/cm^2.

Based on these estimates and on the paramount need to have high-reliability and high-accuracy beam diagnostics, it was decided to implement the LAOR option for the frequency-conversion system. In the final configuration, the blast shield was left uncoated because the expected flux levels were too close to measured damage thresholds for AR coatings. We are investigating the option of coating these optics with Sol-Gel AR coatings (damage threshold ~ 4 J/cm^2).

An overall schematic of the OMEGA system is shown in Fig. 17.2. The six-beam set chosen for 351-nm conversion has near-cubic symmetry.

OMEGA 351-nm Performance

Measurements of the 351-nm conversion efficiency of OMEGA were carried out for over 100 shots. The system (1054-nm) pulse width for the majority of these shots was held at 769±38 ps (FWHM). A compilation of all the single-beam data is shown in Fig. 17.3. The *MIXER*-code[4] prediction of the beam performance is also shown in Fig. 17.3 for comparison. In all shots to date, the experimentally measured, 351-nm conversion agrees well with that predicted by *MIXER*. A total 351-nm energy in excess of 388 J was produced; 30 shots produced a total 351-nm energy in excess of 250 J.

Fig. 17.3
Summary of OMEGA 351-nm performance of individual beams. All beam data is shown here for the input pulse-width range 769±38 ps. Note the close agreement between the measured conversion and the MIXER[4] *code prediction. The extrapolated output energy for a full 24-beam system is given by the scale on the right.*

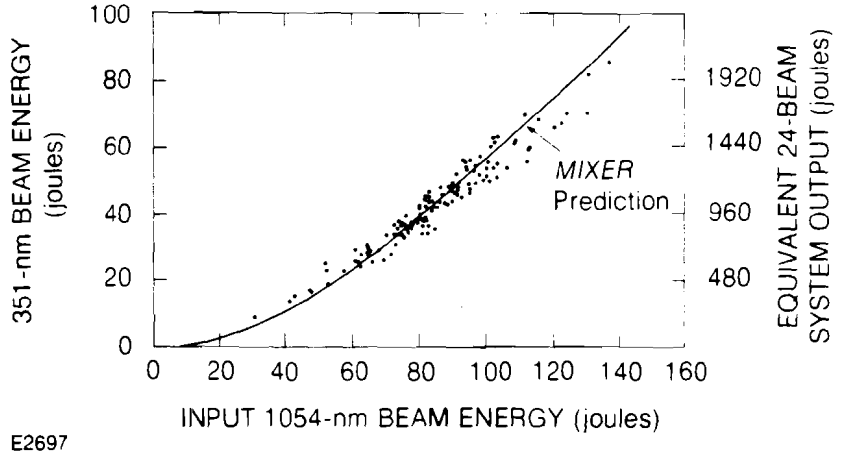

Near-Field and Equivalent-Target-Plane Diagnostics

To measure the equivalent-target-plane energy distribution at 351 nm and compare it to the distribution at 1054 nm, we constructed the system shown schematically in Fig. 17.4. This system makes use of a 10-m-focal-length lens to produce images of both the 351-nm and 1054-nm light at various positions along the focal axis.

A full equivalent-target-plane analysis of the 351-nm distribution is shown in Fig. 17.5. The nonuniformity modulation at both 351 nm and 1054 nm is comparable ($\sigma_{rms} \sim 27\%$). The intensity histogram in this figure shows that for the particular conditions of this shot (energy = 65.2 J, pulse width = 575 ps, and focus position = 1600 μm from best focus), the mean on-target intensity is 10^{14} W/cm^2, and the peak intensity is 1.74×10^{14} W/cm^2.

The near-field, 351-nm and 1054-nm beam distribution has also been recorded for the converted OMEGA beams. Figure 17.6 shows 351-nm, near-field data taken on the same beam as that of Fig. 17.5. The remarkable degree of uniformity ($\sigma_{rms} \sim \pm 8\%$) is a result of the high degree of alignment stability and optical quality of the OMEGA beams.

Fig. 17.4
Schematic of the two-wavelength equivalent-target-plane system used to produce both 351-nm and 1054-nm images of the beam at various positions along the focal axis.

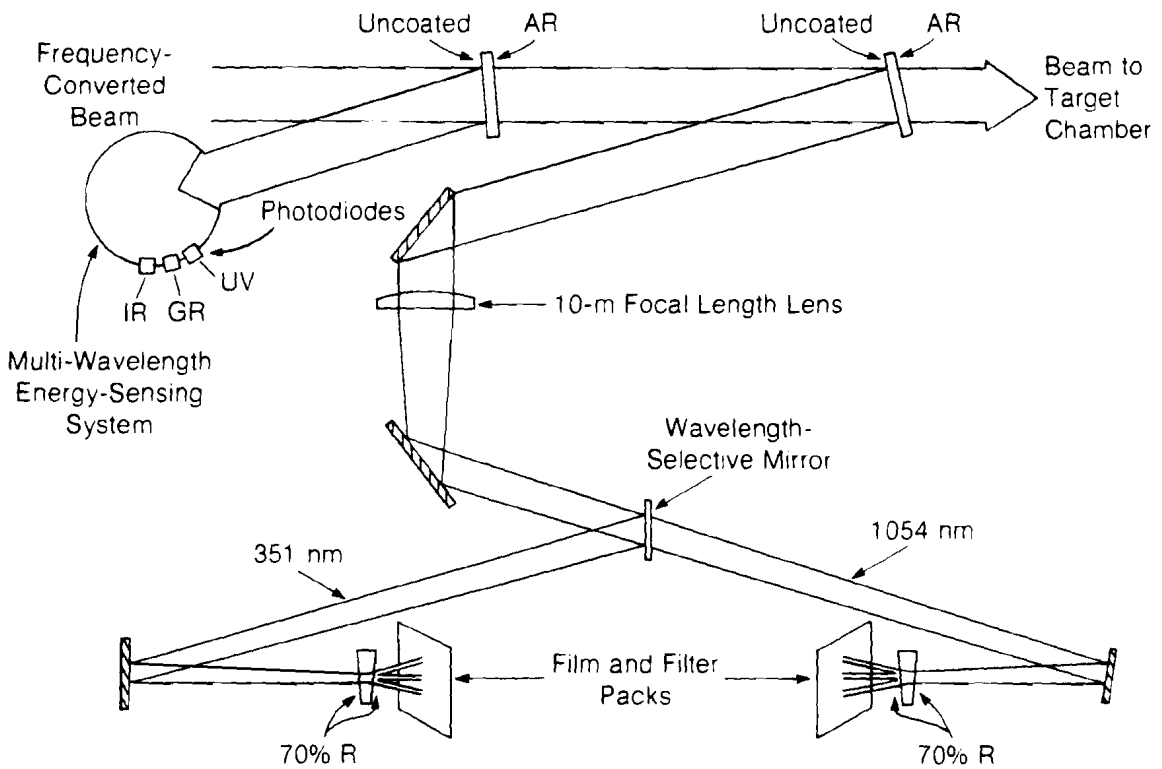

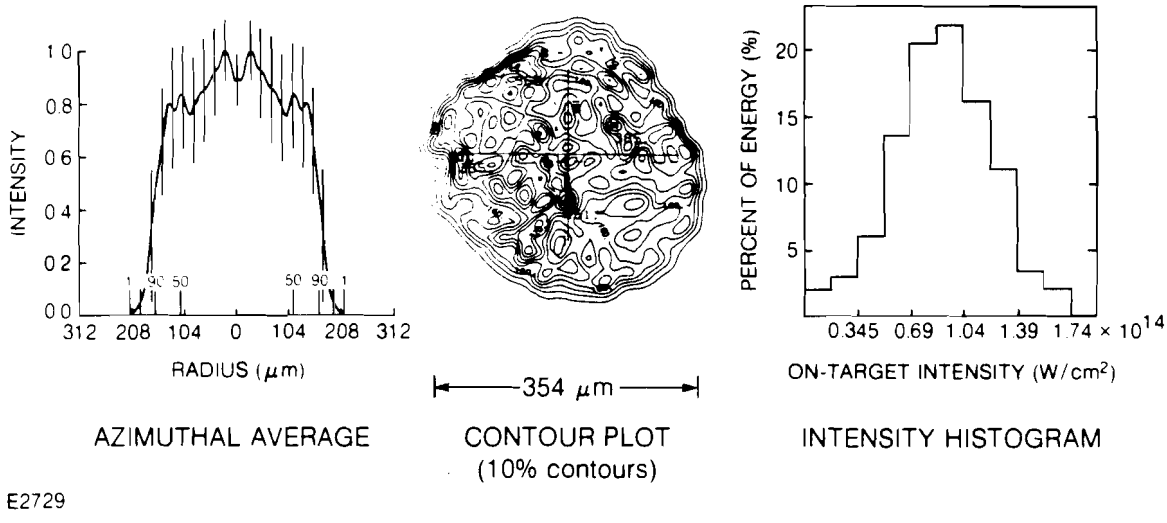

Fig. 17.5
Analysis of the equivalent-target-plane energy distribution for a single 351-nm beam at 1600 μm from best focus. A 719-ps IR pulse is converted to the 575-ps, 65.2-J UV pulse shown.

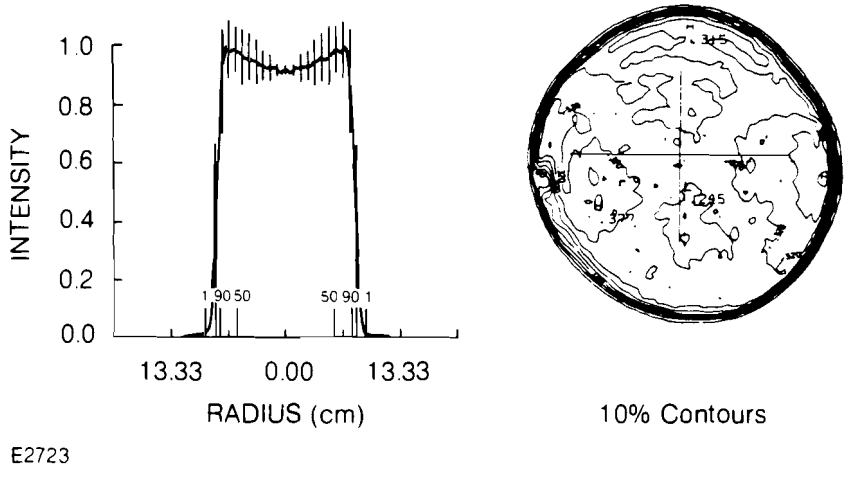

Fig. 17.6
Near-field photograph and analysis for the same beam as in Fig. 17.5 at an output-energy level of 58.8 J (351 nm).

Alignment System

Early in the design deliberations for the OMEGA conversion, it was decided to maintain the 1064-nm alignment capability of the converted system and, in fact, to try to do the full target alignment at 1064 nm. The use of auxiliary 351-nm lasers for multi-beam alignment was considered too expensive and unreliable. The transport optics were, therefore, specified to be two-wavelength capable (351 nm and 1064 nm).

The primary complications of doing 351-nm alignment with a 1064-nm beam are (a) chromatic shift and chromatic aberrations in the focus lens and (b) fundamental and second-harmonic rejection at the target plane.

In considering the first issue, two competing designs were calculated for the focusing optics. One of the designs was a single-element aspheric lens, and the other was a two-element aspheric/aplanat. It was found that the single-element aspheric design would have 1.2 waves of single-pass wavefront distortion at 1064 nm, compared with 0.25 waves at 351 nm, and that the two-element lens could produce diffraction-limited performance at both wavelengths. The consequence of the high wavefront distortion of the single-element design at 1064 nm is a poor focal resolution at this wavelength. We estimated that the focal resolution of the single-element lens would be $\pm 100\,\mu$m, compared to $\pm 25\,\mu$m for the two-element lens. To confirm these estimates, we performed a test with a 14-cm, f/3, quartz aspheric lens designed for 351-nm operation. We found that even though the depth of field was about $100\,\mu$m to $200\,\mu$m at 1064 nm, an operator could reproducibly focus the lens at 1064 nm to within $\pm 12\,\mu$m of a given location. The same operator could focus a diffraction-limited lens to similar accuracy. As a result of this study, we implemented single-element aspheric lenses on OMEGA.

The second issue, 1054-nm and 527-nm rejection at the target plane, was resolved very easily. The blue-beam focus of the 600-mm, single-element aspheric lens is approximately 34 mm ahead of the red-beam focus. Under most anticipated target conditions, the resulting intensity at 1054 nm is 10^{-3} of that at 351 nm. While solving the color separation problem, this large chromatic shift introduces some additional alignment problems, i.e., maintaining pointing stability as the lens is translated from red focus to blue focus. To solve this problem, we made use of the intrinsic high accuracy of the existing OMEGA lens holders. We installed a pneumatically driven ram to provide the large-scale shift between red and blue focus, and we used the existing fine adjustment to provide precision travel over 4 mm. Tests of the pointing resolution and stability and of the focus-position resolution and stability were carried out using x-ray imaging. From these measurements, we inferred a pointing accuracy and stability of $\sim \pm 10\,\mu$m and a focusing resolution and stability of $\leq \pm 50\,\mu$m. This level of accuracy in focus pointing and stability is similar to that previously reported for the 24-beam, 1054-nm operation of OMEGA.

Summary

We have shown in this section that we have met or exceeded all of the DOE laser performance criteria, namely:

(a) We have produced in excess of 388 J in six beams at 351 nm at a pulse width in excess of 0.6 ns, we have taken 30 shots with six-beam energy in excess of 250 J, and we have on-target energy in excess of 298 J.

(b) The measured conversion for the system agrees with *MIXER*[4] calculations to within 10%.

(c) We have measured and successfully evaluated the equivalent-target-plane intensity distribution in both the UV and the IR. A high degree of uniformity is obtained.

(d) We have verified that the system-pointing accuracy and stability is $\pm 10\,\mu$m and that the focusing resolution and stability is $\leq \pm 50\,\mu$m. The comparable 1054-nm numbers are $\pm 11\,\mu$m and $\leq \pm 50\,\mu$m respectively.

ACKNOWLEDGMENT

This work was supported by the U.S. Department of Energy Office of Inertial Fusion under contract number DE-AC08-80DP40124 and by the Laser Fusion Feasibility Project at the Laboratory for Laser Energetics which has the following sponsors: Empire State Electric Energy Research Corporation, General Electric Company, New York State Energy Research and Development Authority, Northeast Utilities Service Company, The Standard Oil Company, and University of Rochester. Such support does not imply endorsement of the content by any of the above parties.

REFERENCES

1. LLE Review **13**, 30 (1982); **16**, 5 (1983).
2. J. Bunkenburg *et al.*, *IEEE J. Quantum Electron.* **QE-17**, 1620 (1981).
3. J. A. Abate, R. Roides, S. D. Jacobs, W. Piskorowski, and T. Chipp, to be published in *Proceedings of the 14th Annual Symposium on Optical Materials for High Power Lasers*, NBS, Boulder, CO, November 1982; F. Rainer and T. F. Deaton, *Appl. Opt.* **21**, 1722 (1982).
4. R. S. Craxton, *Opt. Commun.* **34**, 474 (1980).

Section 2
PROGRESS IN LASER FUSION

2.A Absorption and Hot-Electron Generation Measurements with Spherically Illuminated Targets at λ=351 nm

This section describes the measurements of laser-energy absorption and hot-electron production made on spherical targets irradiated with the six UV beams of OMEGA. These measurements have been conducted over a wide range of parameters. Incident energies in the range 160-298 J, with pulse durations of 600-700 ps, provided intensities across the range of 10^{13}-2×10^{15} W/cm^2. The focus condition was varied between F = -1R (surface-focus condition) through tangential focus (F = 8R) to well beyond tangential focus (F = 11R). Absorption was measured on solid spheres of various materials (CH, Al, Ti, and Ni), having diameters in the range of 80-1200 μm. The principal diagnostic of absorption was an array of 20 differential plasma calorimeters located uniformly around the target. Additional data was also provided by two charge collectors positioned 75 cm and 175 cm from target and a 15-channel x-ray continuum spectrometer monitoring x-ray emission from 1-300 keV.

The absorption fraction as a function of the focus position of the beams is shown in Fig. 17.7. Measurements were made between F = +5R and F = +11R on 400-μm-diameter CH spheres with incident energies of ~ 200 J. At nominal tangential focus (F = +8R) for the f/3.6 beams, the absorption is 80% at an incident intensity of 6×10^{13} W/cm^2. At F = 5R, beyond the limit for the minimum beam overlap on the target, the absorption is not significantly greater. However, at F = 11R the laser beam overflows the target, and refractive losses are significant. Consequently, the absorption is markedly reduced (~ 60%).

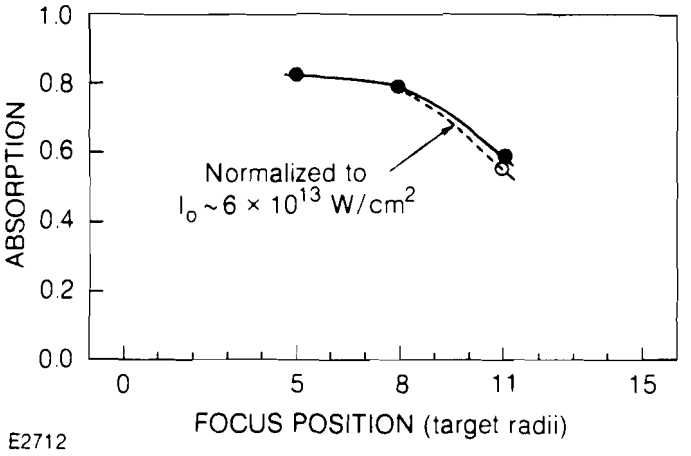

Fig. 17.7
Absorption for 400-μm-diameter CH spheres for different focus parameters and for ~200-J, 650-ps pulses. The circle represents the result estimated for the same average on-target intensity at F = +11R as at the other focal positions. This correction involves a normalization of the absorption efficiency according to measured intensity dependences.

Correction of this net absorption value for the reduced average intensity resulting from the overflow and refraction losses, and, therefore, for the higher absorption efficiencies known to occur at lower intensities, decreases this value further. Thus, although higher uniformity is probably obtained with six beams focused beyond the tangential limit, this is only achieved at the expense of absorption. Consequently, all the parametric scaling of absorption was made for tangentially focused beams.

Figure 17.8 shows the variation of absorption with intensity for CH spheres varying in diameter between 100 μm and 420 μm for incident energies of the order of 200 J. It can be seen that the overall absorption drops from ~80% at low intensities to values of the order of 40% at intensities approaching 10^{15} W/cm^2. Although subsequent data will establish that the principal absorption mechanism throughout

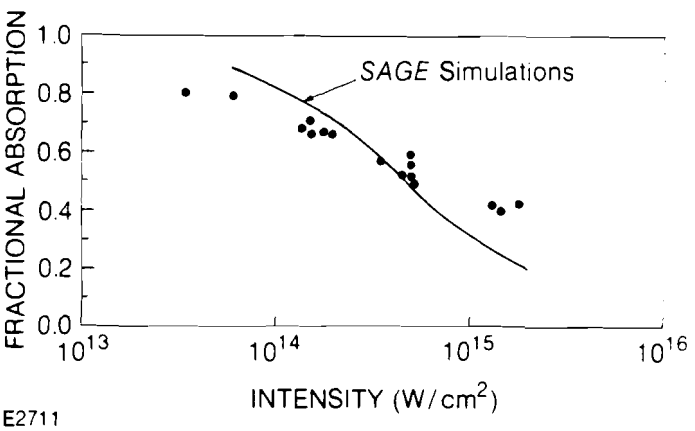

Fig. 17.8
Ultraviolet absorption for tangentially focused (F = +8R) E_L = 160-298 J, t_L = 600-650-ps pulses on targets with radii in the range 45-220 μm, all with > 2-μm CH outer layers. The SAGE *simulation curve is for 200-J, 600-ps pulses, assuming a flux-limit parameter f=0.04.*

this range is inverse-bremsstrahlung absorption, the reduced absorption at high intensity is affected by the smaller target size (i.e., the small scale length). For the higher incident energies expected from full conversion of OMEGA to 351 nm, significantly higher absorption should be obtained at these intensities. Figure 17.8 also shows a comparison of the experimental data with one-dimensional *SAGE* calculations made assuming a flux-limiting parameter of f = 0.04. As can be seen, absorption significantly higher than predicted is obtained at high intensities, whereas at lower intensities the absorption is less than predicted. Although not plotted, a similar discrepancy exists between the experimental data and the predictions of the one-dimensional Lagrangian code, *LILAC*.

Figure 17.9 shows the absorption as a function of intensity for targets of various Z. Solid targets of aluminum, nickel, and titanium were shot at various intensities in the range 10^{13}–10^{15} W/cm^2 with incident energies in the range 160-180 J. Measured absorption in excess of 95% was obtained at an intensity of 1.1×10^{13} W/cm^2. This measurement incidentally confirms the energy calibration between the plasma calorimeters and the optical calorimeters measuring output beam energy. The absorption on high-Z targets is somewhat greater than that on CH targets for comparable intensities, in agreement with previous measurements made on planar targets with GDL.[1]

Measurements of hot-electron generation were obtained from x-ray continuum spectra from solid spherical targets irradiated with the six-beam ultraviolet OMEGA system. Estimates of the electron density and temperatures are found to show reasonable agreement with data obtained from the one-beam UV target experiments on GDL[2] and to support the argument that no significant preheat levels are evident in

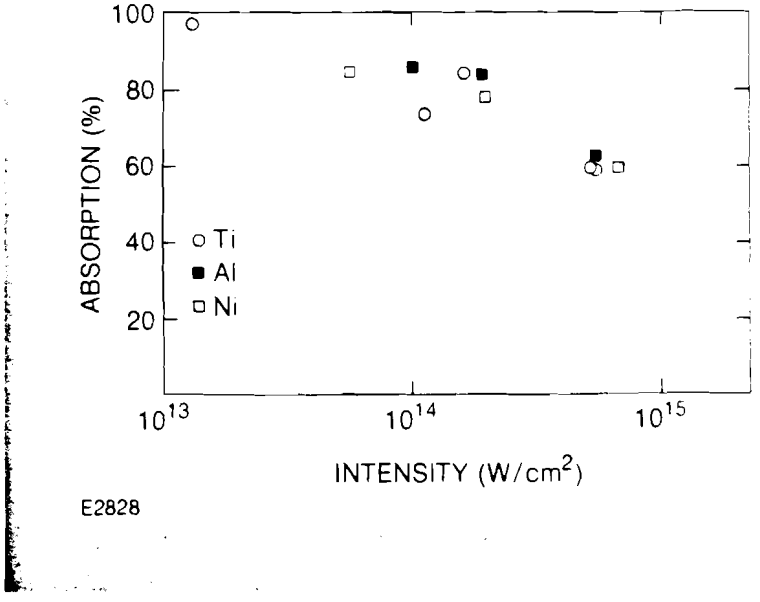

Fig. 17.9
Absorption measurements using high-Z targets of various materials and radii (40-600 μm) with pulses (E_L = 160-180 J, t_L = 600-640 ps) at tangential focus (F = +8R).

spherical UV experiments, as compared to IR experiments. Incident energies in the range 160-200 J with pulse durations of 600-700 ps provided intensities across the range of 6×10^{13} – 2×10^{15} W/cm^2 at tangential focus (F=8R). The targets used were solid spheres having diameters of 80-420 μm. The data to be shown here are from targets with a minimum of 4 μm of CH over CH, Al, Ti, or Ni. To first order, hot-electron density and temperature scaling were obtained over similar ranges of intensity as the absorption measurements.

The principal diagnostic for measuring the level of hot-electron generation was a multichannel x-ray continuum spectrometer consisting of 9 PIN diodes and 6 PM-NaI scintillator detectors in conjunction with a wide variety of K-edge x-ray filters. The detector arrays incorporated lead collimators and shields to minimize pick-up of x rays from the target chamber walls. The PM detectors were calibrated using nuclear sources, and the sensitivity of the silicon diodes was obtained from known calibrations. The charge pulses from the detectors were integrated and recorded using gated analog-to-digital recorders. Additional oscilloscope monitoring was used to check for noisy or saturated signals. Table 17.1 shows the detectors and filters used. Since the individual detectors do not sample discrete energy bands in the x-ray spectrum, an interpolation approach to the estimation of the $dE/dh\nu$ curve is used. The approach taken in this work uses a multi-Maxwellian model to approximate the data. The spectrum is thus obtained globally rather than locally, the signals from individual detectors consequently contributing to broad regions of the spectrum. The points shown in the spectra correspond only to

Table 17.1.
OMEGA K-edge-filtered detector-system parameters.

Filter Material	Filter Thickness	K-Edge (keV)	Detector Material	Detector Thickness	Detector Type
Cl (Saran)	50 μm	2.8	Si	250 μm	PIN
Sc	28	4.5	Si	250	PIN
Fe	25	7.1	Si	250	PIN
Ni	20	8.3	Si	250	PIN
Zn	47	9.7	Si	250	PIN
Y	253	17.0	Si	250	PIN
Mo	113	20.0	Si	250	PIN
Ag	136	25.5	Si	250	PIN
Ag	254	25.5	NaI	1 mm	PMT
Sn	250	29.2	NaI	1	PMT
Ta	507	67.4	NaI	1	PMT
Pb	1.0 mm	88.0	NaI	1	PMT
Pb	2.5	88.0	NaI	50	PMT
Pb	5.7	88.0	NaI	50	PMT

E2839

the peak of the sensitivity window for each detector and consequently change in energy for a different spectrum. (See LLE Review, Volume 13, for further details on this approach.[2])

A typical spectrum obtained from a CH sphere irradiated at high UV intensity by the six beams of OMEGA is shown in Fig. 17.10(b). During the course of these experiments, it has generally been found that the x-ray continuum spectrum from UV-irradiated spherical targets can be satisfactorily fitted with a two-component Maxwellian spectrum, as is shown in the figure. The spectrum in Fig. 17.10(b) was obtained at an incident intensity of approximately 2×10^{15} W/cm^2. The low-temperature, low-energy Maxwellian distribution corresponds well to the x-ray emission expected from the 0.8-keV thermal plasma, and the low-level, high-energy, high-temperature (~25-keV) spectrum is evidence of the existence of a suprathermal, collisionless electron component in the plasma.

In comparing the x-ray spectrum obtained with UV radiation on OMEGA at similar intensities to those measured in earlier IR experiments on OMEGA, a strong difference in the character of the

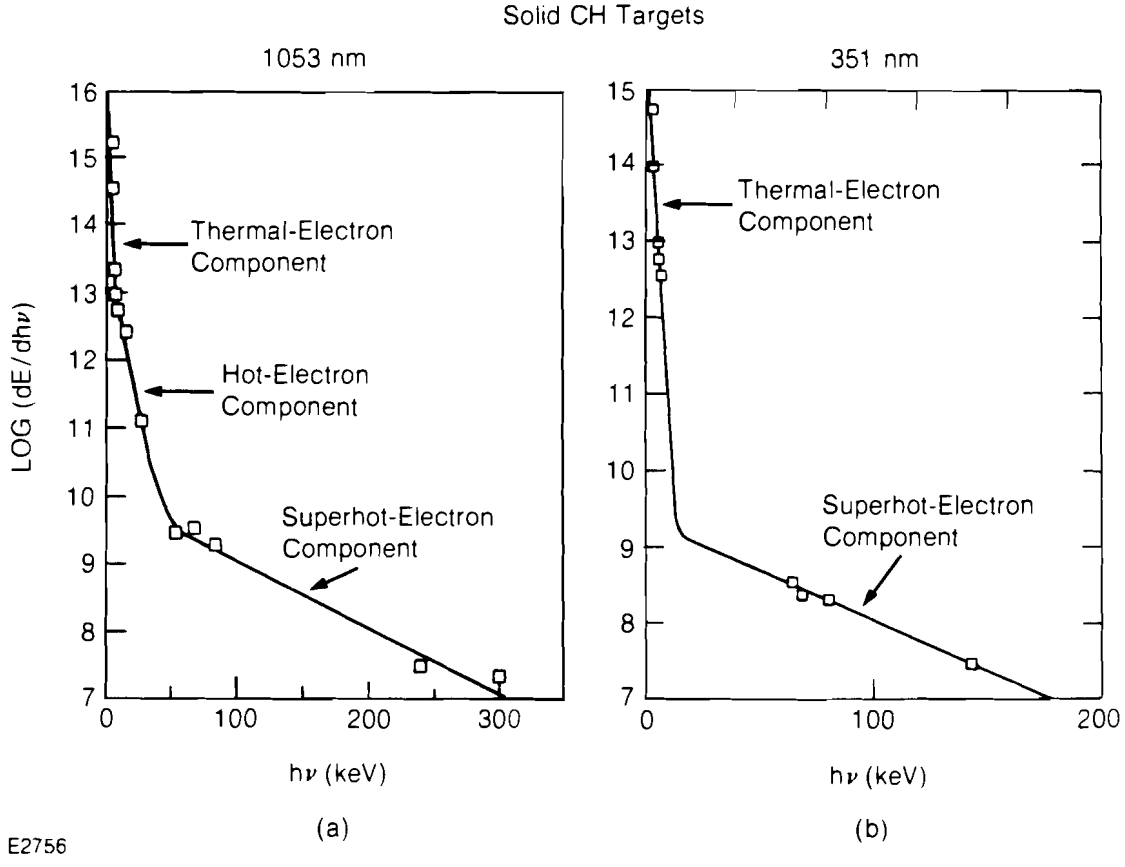

Fig. 17.10
X-ray continuum spectra from spherical targets obtained with (a) the 24-beam OMEGA system at λ=1053 nm and (b) the six-beam OMEGA system at λ=351 nm.

spectrum is observable [Figs. 17.10(a) and 17.10(b)]. Infrared irradiation of spherical targets at intensities of 10^{14}-10^{15} W/cm^2 with nanosecond pulses always resulted in the emission of a three-component spectrum comprised of a thermal electron component, a hot-electron component resulting from resonance absorption at critical density, and a superhot component resulting from hot-electron generation in the underdense corona. The two-component spectrum observed in all spherical UV experiments on OMEGA is clear evidence of the absence of resonance absorption in the interaction. This difference in the x-ray continuum spectrum between UV and IR irradiation in spherical geometry was previously observed in planar geometry on GDL.[7]

The relative partition of energy in the superhot-electron component for UV irradiation of spherical targets, as a function of intensity, is shown in Fig. 17.11(a). This shows the ratio of the energy in the suprathermal tail of the distribution, normalized to the incident energy, as a function of incident irradiance, for CH targets of diameters ranging between 90 and 440 μm. Although the data, particularly at lower intensities, shows considerable scatter, the general form of the intensity dependence is clear. At low intensities, the partition of energy to superhot electrons is extremely small and displays a sharp onset at an intensity ~10^{14} W/cm^2. Moreover, at high intensities, there is clear indication under the prevailing conditions of a saturation in the conversion to superhot electrons at a level below 10^{-3}. Again, this data is remarkably similar to the earlier planar GDL results shown in Fig. 17.11(b).

Fig. 17.11
Fraction of absorbed energy in the superhot-electron distribution with 351-nm illumination with (a) the six-beam OMEGA system and (b) the one-beam GDL system.

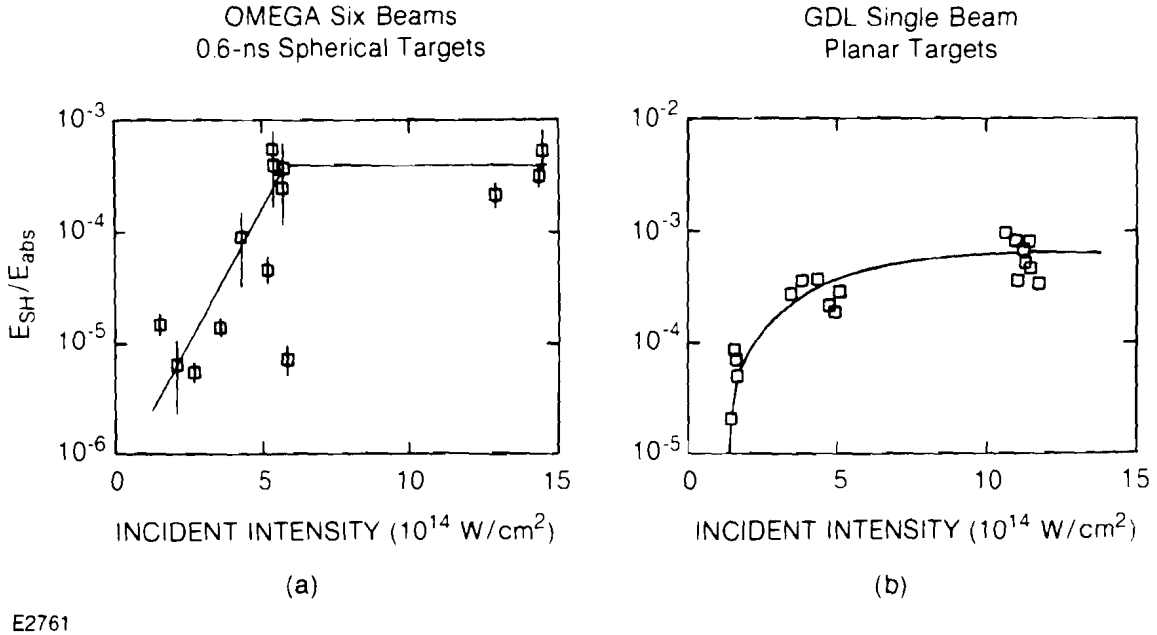

Plotted in Fig. 17.12 is the intensity dependence of the conversion efficiency to hot electrons (resulting from resonance absorption) measured in spherical IR experiments and the conversion efficiency to superhot electrons (from subcritical phenomena) measured in both IR and UV spherical experiments. Although the x-ray continuum spectrum overestimates the conversion of energy to hot electrons for IR experiments, the clear absence of resonance-absorption-generated hot electrons in UV spherical experiments clearly implies vastly reduced preheat levels for UV radiation.

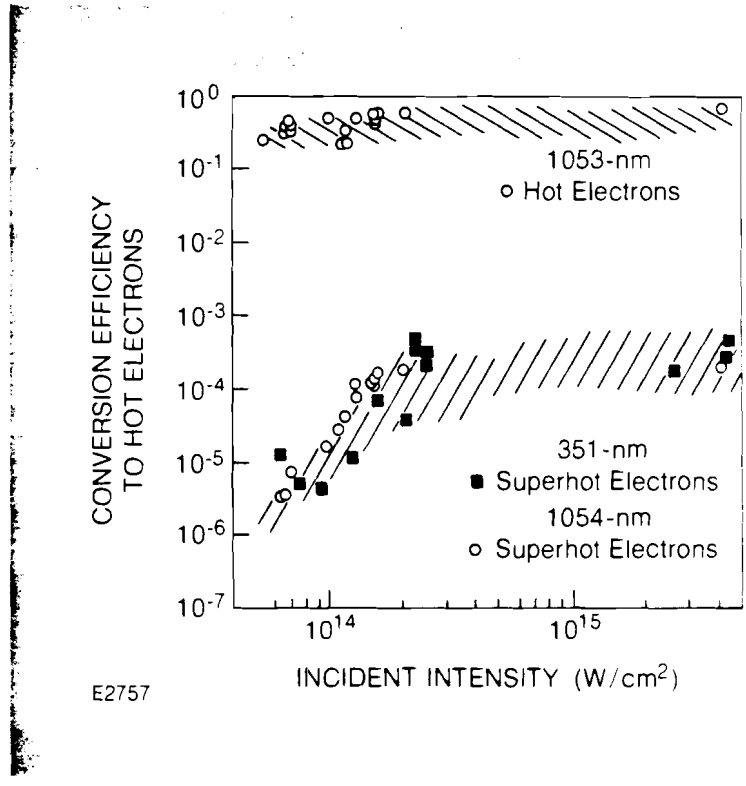

Fig 17.12
Fraction of absorbed energy in various hot-electron components at illumination wavelengths of 1053 nm and 351 nm. Because the hot component is absent at 351 nm, the total hot-electron preheat is substantially reduced at 351 nm.

Comparison of the level of hot-electron generation and the level of $3\omega_0/2$ harmonic emission provides some indication of the origin of the suprathermal electrons in UV-irradiated spherical plasmas. This comparison is shown in Fig. 17.13. As can be seen, there is a clear correspondence in the intensities at which both this harmonic and the generation of hot electrons commence in their similar intensity dependences. Moreover, saturation in the harmonic emission and in the suprathermal electron generation appears to occur at a similar intensity (~10^{15} W/cm^2). Since there is strong evidence that the $3\omega_0/2$ harmonic emission originates from the $2\omega_p$ instability, this close correspondence in intensity dependence suggests strongly that the suprathermal electrons have a similar origin.

Summary

The measurements of the absorption, electron density, and temperature characteristics of UV-irradiated plasmas at high intensity show reasonable agreement with previous planar-target data and indicate significantly higher absorption and significantly lower preheat levels for UV irradiation, compared to IR experiments.

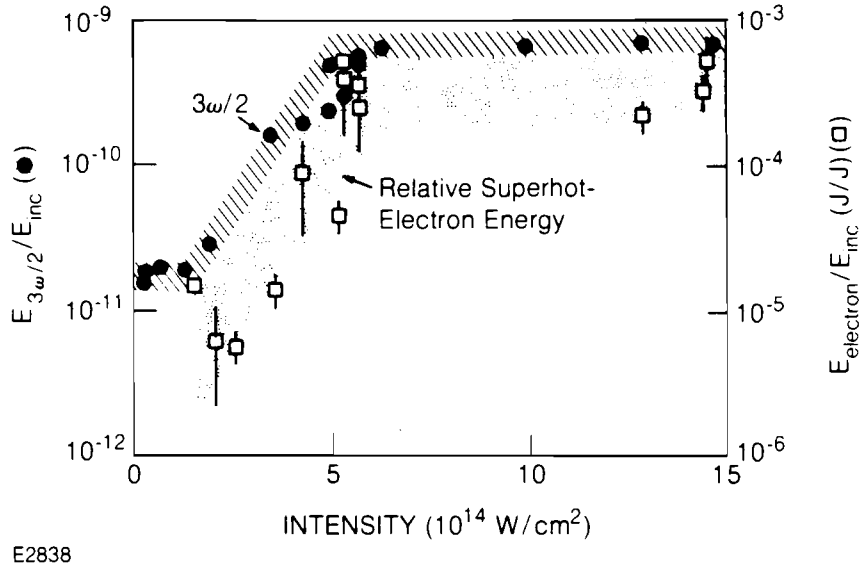

Fig. 17.13
Comparison of the energy in superhot electrons and 3/2-harmonic emission. The remarkable similarity in the curves strongly suggests that the superhot electrons are produced by the $2\omega_p$ instability.

ACKNOWLEDGMENT

This work was supported by the U.S. Department of Energy Office of Inertial Fusion under contract number DE-AC08-80DP40124 and by the Laser Fusion Feasibility Project at the Laboratory for Laser Energetics which has the following sponsors: Empire State Electric Energy Research Corporation, General Electric Company, New York State Energy Research and Development Authority, Northeast Utilities Service Company, The Standard Oil Company, and University of Rochester. Such support does not imply endorsement of the content by any of the above parties.

REFERENCES

1. W. Seka, R. S. Craxton, J. Delettrez, L. M. Goldman, R. Keck, R. L. McCrory, D. Shvarts, J. M. Soures, and R. Boni, *Opt. Commun.* **40**, 437 (1982).
2. LLE Review **13**, 23 (1982).

2.B Parametric Instabilities in Underdense Spherical Plasmas with λ=351 nm Illumination

The six-beam ultraviolet OMEGA coronal physics program is motivated by the fact that all energy input to laser-fusion targets occurs within the coronal plasma. In this region, the bulk of the laser energy is absorbed through inverse-bremsstrahlung (collisional) absorption. The coronal plasma, heated to temperatures of 1 to 3 keV, expands into the vacuum and by reaction compresses the core of the target. A very high compression is essential for the success of laser fusion, and the quality of the compression depends critically on many parameters in the plasma corona.

Laser light of frequency ω_0 incident on a spherical target is absorbed on its way to the critical-density surface mostly by collisional absorption. A small part of the incident energy is also channeled into a host of parametric instabilities,[2] most notably the $2\omega_p$ decay instability at the quarter-critical ($n_e = n_c/4$) surface, where laser photons decay into plasmon (plasma-wave) pairs of frequency $\omega \approx \omega_0/2$, which is the local plasma frequency of the quarter-critical surface. This region then becomes a source of energetic electrons (superhot electrons), as well as a number of half-integer harmonics of the incident laser light ($\omega_0/2$, $3\omega_0/2$, $5\omega_0/2$, etc.).

Light penetrating up to the critical-density ($n_e = n_c$) surface can be absorbed in that region through resonance absorption. This process is dominant for long-wavelength irradiation, but for 351-nm irradiation at pulse lengths longer than 100 ps, no evidence for resonance absorption has been found.[1]

Until recently, most UV-laser-plasma interaction experiments were carried out with a single beam incident on flat targets. A large data base has been collected, and most diagnostics indicate a strongly two-dimensional (2-D) behavior of these plasmas. In particular, self-focusing of the laser light is found to abound under these conditions at incident intensities above 5×10^{13} W/cm^2.[3-7] In contrast, uniformly illuminated spherical targets are expected to exhibit a much more one-dimensional (1-D) character allowing for much easier interpretation of many of the plasma-physics effects occurring in the corona.

The diagnostics used in these experiments are mostly optical and x-ray spectroscopy. The latter serves as an energetic-electron monitor, while the former can give detailed information on the specific parametric processes occurring in the corona. Furthermore, these visible spectra can serve as a valuable coronal diagnostic for the electron temperature at various locations in the plasma.

A schematic coronal electron-density profile is shown in Fig. 17.14, along with the various parametric processes and their ramifications, in terms of hot-electron generation and optical signatures. The critical-density processes like resonance absorption and parametric decay are seen clearly in OMEGA infrared experiments through careful analysis of the $2\omega_0$ and x-ray spectra from these plasmas.[5] So far, we have been unable to investigate any $2\omega_0$ spectra in our UV experiments, but the continuum hard x-ray spectra show no evidence for resonance absorption.

The $2\omega_p$ decay instability at $n_c/4$ is observed both in its optical signals and in the x-ray signature of the superhot electrons generated by this instability. Evidence for stimulated Brillouin scattering (SBS), an instability in which the incident laser light decays into an ion-acoustic wave and an electromagnetic wave,[4] is found in the highest-intensity OMEGA shots only. However, the SBS levels observed even in these cases are negligibly small. Most recently, optical spectra have been observed on OMEGA which have traditionally been attributed to stimulated Raman scattering (SRS) below $n_c/4$, where an incident

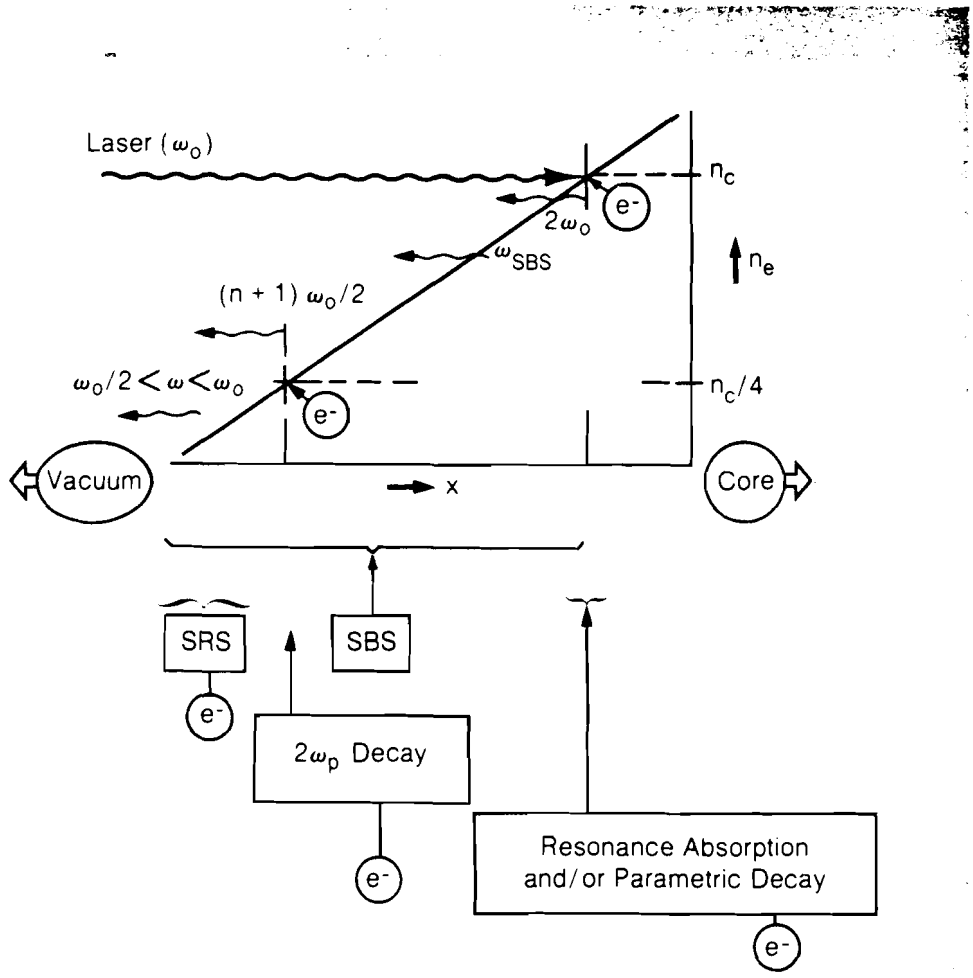

Fig. 17.14
Schematic plot of the coronal electron density profile showing where the various parametric processes occur. The plot shows the characteristic electromagnetic signals generated by the parametric process labelled beneath the plot. The generation of energetic electrons, chiefly through the damping of electron plasma waves, is indicated by a circled "e⁻."

photon decays into a plasmon and a scattered photon, but from threshold considerations, this instability should not be excited at intensities below 10^{15} W/cm^2 where the experiments were conducted. We are presently studying these spectra as well as novel theoretical models for their interpretation.

Figure 17.15 is a schematic layout of the coronal diagnostics employed in the new multibeam experiments. The light scattered by the target near the fundamental irradiation frequency ω_0 is analyzed spectroscopically in backscattering and sidescattering. Another spectrometer analyzes the $\omega_0/2$ radiation. Photodiodes with appropriate filters have been absolutely calibrated to measure the light energy scattered at $\omega_0/2$ and $3\omega_0/2$. A camera filtered to photograph the target in the scattered light at $\omega_0/2$ is used to investigate the $\omega_0/2$ emission pattern. X-ray diodes and photomultipliers are used to measure the x-ray continuum spectrum between 2 and 200 keV. Plasma calorimeters are used to measure the amount of laser light absorbed by the plasma.

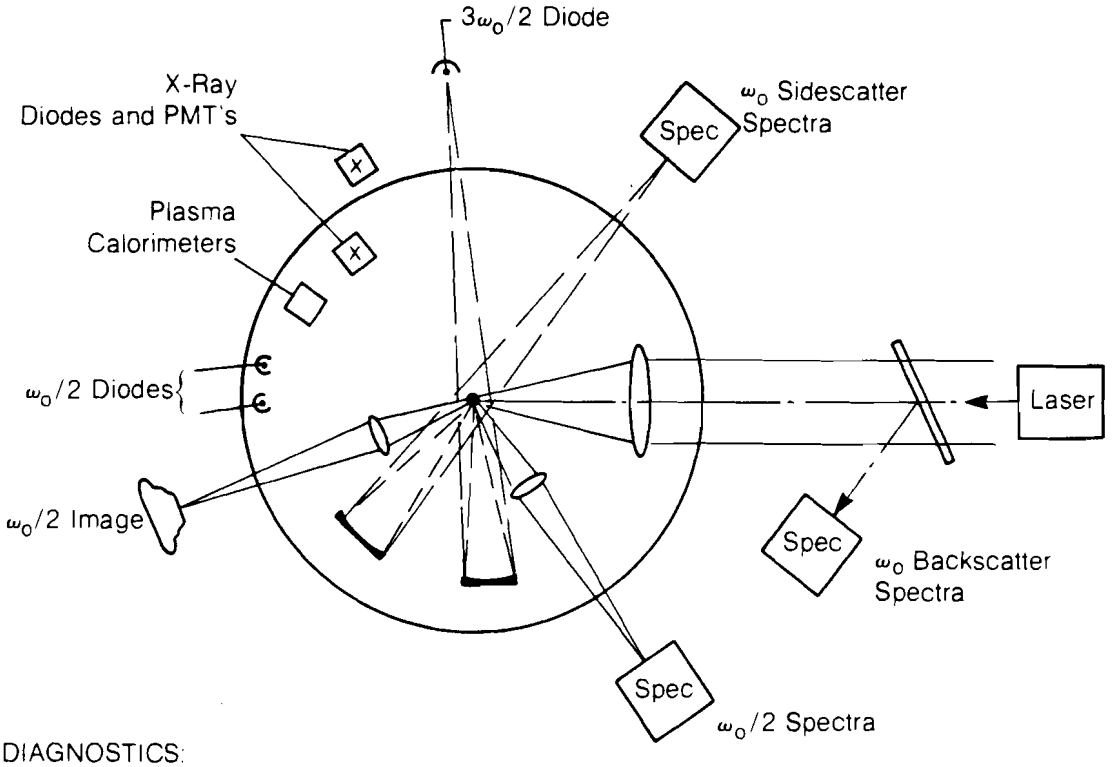

DIAGNOSTICS:

- ω_0 backscatter and sidescatter spectroscopy
- $\omega_0/2$ spectroscopy, diodes, image
- $3\omega_0/2$ diodes
- X-ray diodes and photo-multiplier tubes (PMT's)
- Plasma calorimeters

E2749

Fig. 17.15
Schematic lay-out of diagnostics used in the coronal physics experiments on OMEGA. The spectroscopic diagnostics cover wavelengths from the IR to the hard x-ray region. Reflective optics with dielectric coatings were used for imaging and/or light collection between 200 and 400 nm for ease of alignment and optimum light-gathering efficiency.

Threshold formulae and typical threshold intensities for our UV interaction experiments are shown in Fig. 17.16. While the threshold condition for SBS should be surpassed in most of our OMEGA shots, we have not seen SBS, except in the highest-intensity shots. This is consistent with experiments done elsewhere. The reason for the absence of SBS is not completely clear at this point. The filamentation threshold depends on a number of factors, particularly the degree of uniformity of irradiation. For uniform OMEGA irradiation, the filamentation threshold may be considerably higher than the range of values indicated in this figure. The $2\omega_p$ instability has indeed been found to have a threshold near 2×10^{14} W/cm^2.

- Predicted and Observed Thresholds of Parametric Instabilities -

	Theory W/cm^2	Typical Prediction W/cm^2	Observed W/cm^2
• $2\omega_p$ Decay	$\frac{5 \times 10^{12}\, T_{eV}}{L_{\mu m}\, \lambda_{\mu m}}$	2×10^{14}	6×10^{13}
• SRS-Absolute	$\frac{5 \times 10^{17}}{L_{\mu m}^{3/4}\, \lambda_{\mu m}^{2/3}}$	3×10^{15}	4×10^{14}
• SRS-Convective	$\frac{4 \times 10^{17}}{L_{\mu m} \lambda_{\mu m}}$	2×10^{16}	4×10^{14}
• SBS	$\frac{4 \times 10^{11}\, T_{eV}}{L_{\mu m}\, (n_e/n_c)}$	2×10^{13}	6×10^{13}
• Filamentation		$1\text{-}3 \times 10^{14}$	10^{14}
• Parametric Decay	$\frac{7 \times 10^{11}\, T_{eV}}{L_{\mu m}\, \lambda_{\mu m}}$	2×10^{14}	10^{14}

Typical predictions for: λ = 351 nm, L = 75 μm at $n_c/4$, L = 10 μm at n_c, T = 1 keV

E2624

Fig. 17.16
List of parametric instabilities, their theoretical threshold formulae, and typical theoretical predictions along with experimental thresholds observed in single-beam GDL experiments. While scale lengths between 50 and 75 μm are typical near the $n_c/4$ surface for current UV-laser-plasma experiments, scale lengths around 10 μm are expected near the n_c surface and were used to estimate the parametric decay threshold (last entry in the list above).

Earlier Interaction Experiments at LLE

To set the stage for the new OMEGA results, a short review of the old, single-beam experiments is presented in Figs. 17.17 through 17.20. The common thread in these single-beam experiments is the necessity of resorting to filamentation of the laser beam in the corona to explain the many different experimental results.

Figure 17.17 shows single-beam results for light energy scattered at $\omega_0/2$ (700 nm) and at 480 nm, plotted as functions of irradiation intensity.[8] The former has two steps: the first corresponds to the onset of the $2\omega_p$ instability, and the second corresponds to the absolute SRS instability. The 480-nm signal is related to the convective SRS instability, and it also shows a rapid rise at 4×10^{14} W/cm^2, even though the theoretical threshold for this process is ten times higher than the absolute SRS threshold. Furthermore, the thresholds observed here for the $2\omega_p$ and absolute SRS are themselves too low by factors of 5 to 10. This discrepancy can be explained only by invoking filamentation, for which there are also other indicators (see below).

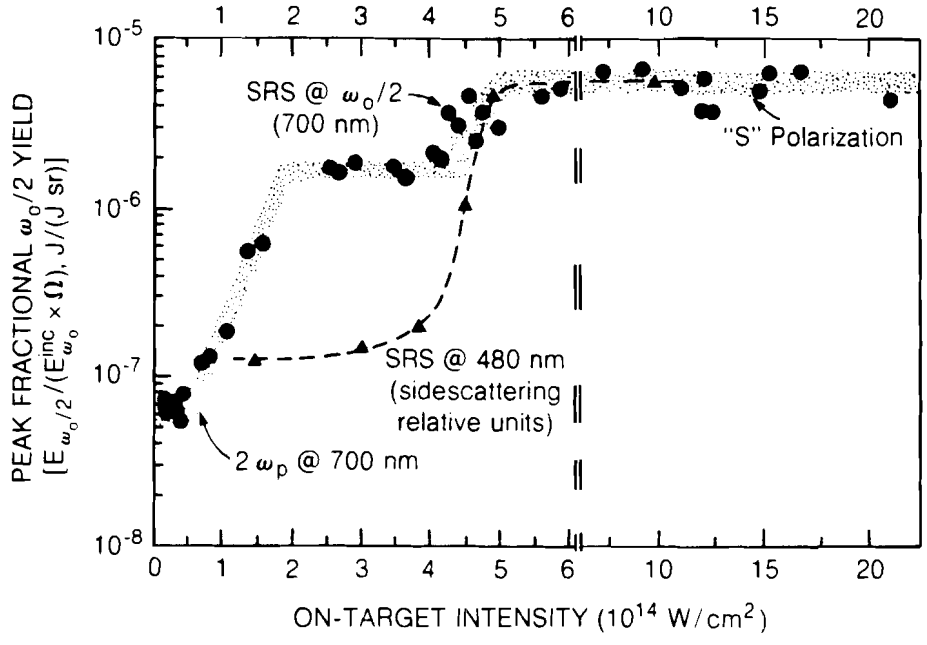

E1521

Fig. 17.17
Light emission from UV-laser plasmas at 700 nm (•) and at 480 nm (▲). Planar CH targets were illuminated with 0.5-ns pulses focused onto spots of varying size (100 to 500 μm). Emission was observed in the same polarization as the incident light. The 700-nm signal at half the laser frequency exhibits two thresholds corresponding to the $2\omega_p$ decay and absolute SRS instability. The 480-nm signal originates from the convective SRS instability and has an observed threshold equal to that of the absolute instability. All thresholds are at variance with those predicted theoretically. Filamentation of the incident laser light in the corona may explain this discrepancy. Note the scale change at 6 × 10^{14} W/cm^2.

The $3\omega_0/2$ spectra have frequently been used as a temperature diagnostic for the corona. However, the theories of the upscatter of laser photons by $2\omega_p$ plasmons usually applied cannot begin to account for the complexity of spectra seen in UV single-beam GDL experiments. Depending on the angle of observation, one sees asymmetric, double-humped spectra or single-line red- or blue-shifted spectra (see Fig. 17.18). The explanation has been found in a detailed analysis of the $2\omega_p$ decay and the $3\omega_0/2$ generation in filaments.[5]

Although the convective SRS threshold is exceedingly high ($\geq 10^{15}$ W/cm^2), we have seen characteristic SRS spectra in single-beam experiments for this instability.[6] Careful analysis of these SRS spectra has enabled us to determine time-resolved electron temperatures as shown in Fig. 17.19. Compared to the work described in Ref. 5, a more complete SRS theory[9] is applied here, leading to somewhat different coronal electron temperatures than those deduced earlier. We note that the deduced temperatures lie below 2-D hydrocode predictions. We have attributed this discrepancy to depleted tails in the electron distribution function, as expected from the theory of inverse-bremsstrahlung absorption. The mere existence of the SRS spectra, however, requires the existence of filaments, inside which the requisite intensities may indeed exist along with anomalously long density gradients.

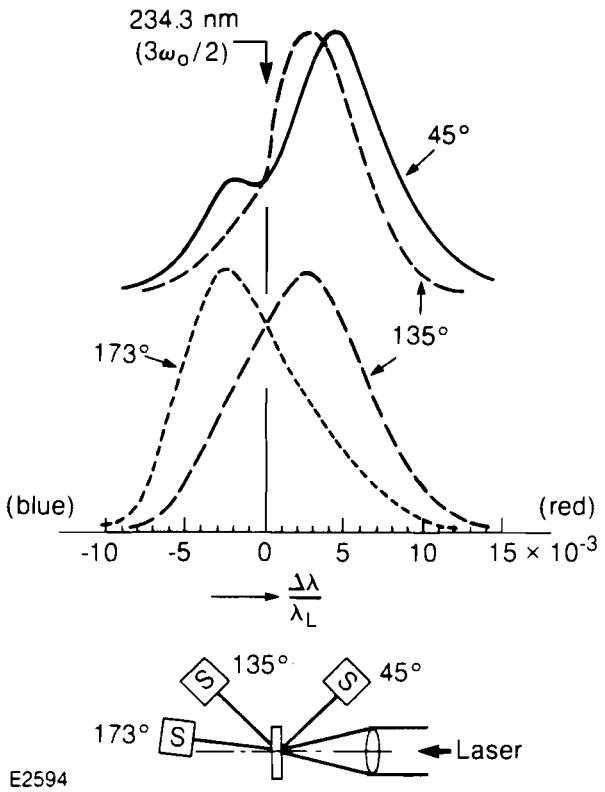

Fig. 17.18
Spectra of the $3\omega_0/2$ emission from thin CH targets for planar 351-nm irradiation. The schematic experimental layout is shown in the lower part of the figure. The various spectra shown refer to different observation angles as indicated. The marked difference between the spectra in the three directions of observation are obvious: they cannot be explained on the basis of the conventional theory of 3/2-harmonic generation. An adequate explanation is given by a model which assumes the $2\omega_p$ decay instability and 3/2-harmonic generation to occur inside self-focusing filaments.

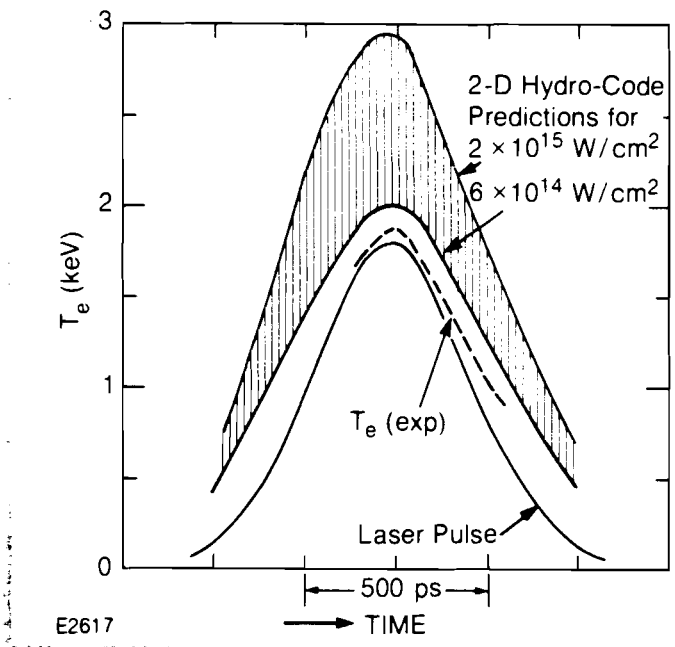

Fig. 17.19
Time-resolved coronal electron temperatures as determined from streaked SRS spectra obtained from 351-nm, 0.5-ns pulses at 10^{15} W/cm² on planar CH targets. Using a recently developed theory by E. A. Williams for the location of the center of gravity of the convective SRS spectrum as a function of coronal electron temperature, we have plotted experimentally deduced electron temperatures (dashed curve). Also shown in this figure are predicted coronal electron temperatures using the 2-D hydrocode SAGE for two different irradiation intensities (solid curves). We note the close resemblance in shape between experimental and simulated electron temperature evolution. A variety of effects may be responsible for the differences observed in the actual values of the temperatures.

Figure 17.20 depicts schematically the various types of scattered light spectra seen near ω_0 in single-beam experiments.[4] Starting from the top of the figure, light seen in transmission is generally unshifted from its original frequency and is Doppler-broadened by the hydrodynamic motion of the plasma it traverses. At oblique incidence, SBS backscatter spectra are observed above a threshold near 10^{14} W/cm^2. The specularly reflected light only suffers slight broadening and negligible shifts, in accordance with expectations for a purely hydro-dominated spectrum. The situation is much more complex at normal incidence. The backscatter spectra show red- and blue-shifted components above a few $\times 10^{14}$ W/cm^2. Analysis of these spectra has shown that filamentation in the corona can also account for these spectra at normal incidence. This does not mean that filamentation only occurs at normal incidence, but it does imply that the filaments must encounter a critical-density layer for the backscatter spectra to show the strong broadening to the blue side of the incident laser frequency.

Fig. 17.20
Schematically depicted spectra of light scattered near the irradiation frequency for single-beam, UV-laser plasmas obtained from planar CH targets. Spectra of transmitted light for thin-target experiments as well as spectra of specularly reflected light in oblique-incidence experiments show little spectral broadening and small or no spectral shifts. This is consistent with shifts and Doppler broadening due to plasma motion. Typical SBS spectra are observed in backscattering from oblique-incidence experiments. At normal incidence, the backscatter spectra are complicated by filamentation effects.

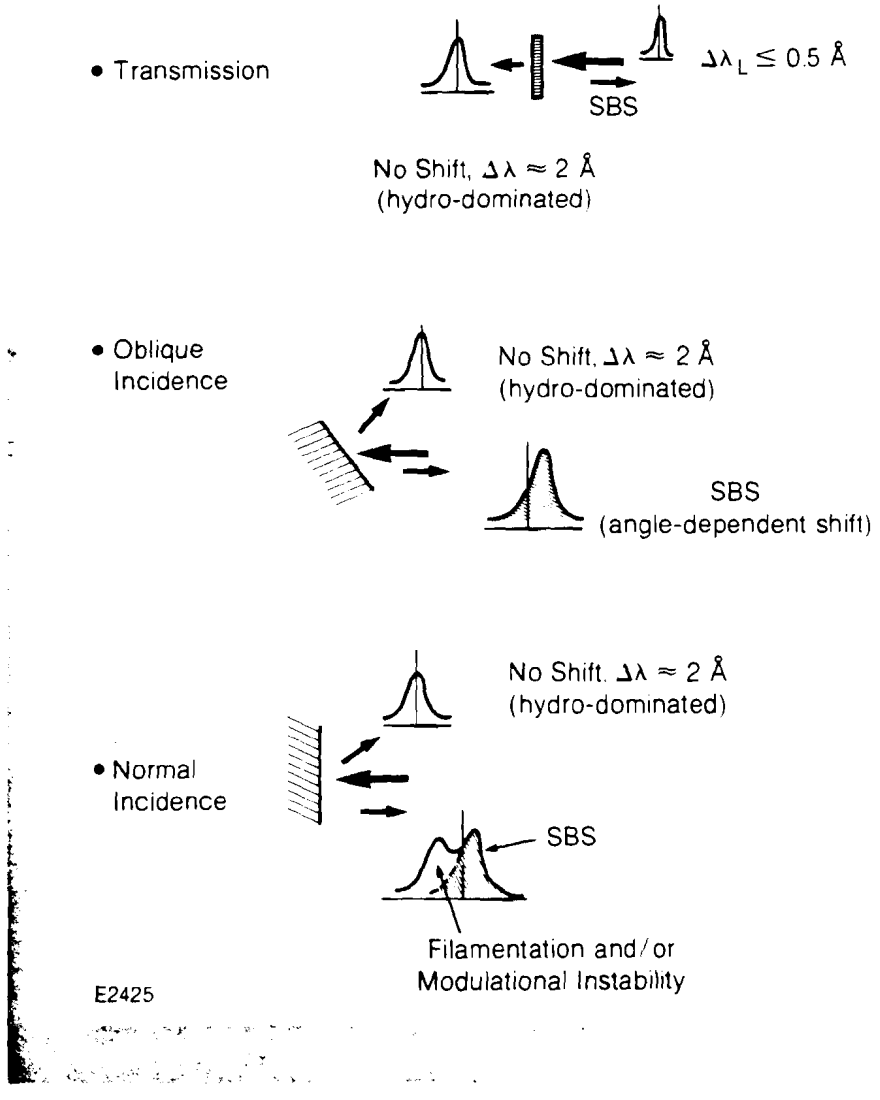

New OMEGA Experiments

The new OMEGA ultraviolet coronal physics results are all characterized by a high degree of reproducibility and an apparent absence of filamentation. At least, none of the experimental data to date require recourse to filamentation to explain their signatures.

The half-harmonic spectrum shown in Fig. 17.21 is typical of a large number of OMEGA shots. Three distinct features are discernible. The dominant sharp line is slightly red-shifted from the $\omega_0/2$ frequency ($2\lambda_L$ wavelength). This line is accompanied by two much broader lines placed approximately symmetrically with respect to $\omega_0/2$. The dashed lines in the figure are drawn to guide the eye. The intensity scaling of all the features as well as the change of the detailed intensity ratios between the various components of the $\omega_0/2$ spectra for different target materials leads us to interpret the spectra in the following way.

The strong, narrow peak is associated with downscattering of the incident photons on the plasmons produced by the $2\omega_p$ decay at $n_c/4$. In this process, the **k**-matching conditions, $\mathbf{k}_s = \mathbf{k}_0 - \mathbf{k}_p$, have to be fulfilled along with the condition $\omega_s = \omega_0 - \omega_p$. Here, $\mathbf{k}_0$, ω_0 and $\mathbf{k}_s$, ω_s are the wave vectors and frequencies of the incident and scattered electromagnetic wave, and $\mathbf{k}_p$, ω_p are the wave vector and frequency of the plasma wave. It can be shown from the photon and plasmon dispersion relations that these matching conditions are satisfied for only a very narrow range of **k**'s, which leads to the sharp line shown in Fig. 17.21. Furthermore, the red shift of this line is well-defined for the same reason and may be written as $\Delta\lambda = 31 \times T_{e\ keV}$. This relation is obtained from recent work on the $2\omega_p$ decay instability.[5,10]

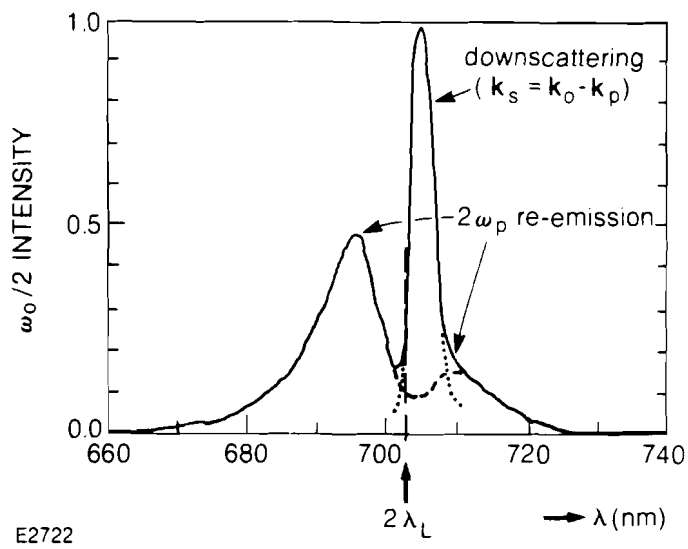

Fig. 17.21
Half-harmonic ($\omega_0/2$) spectra from spherical six-beam, UV-laser plasmas obtained using 4×10^{14} W/cm² illumination. A typical, highly reproducible, half-harmonic spectrum obtained on OMEGA using a spherical CH target is shown. The dashed and dotted lines are shown to help distinguish the underlying spectral features. The sharp spike is due to ordinary (non-stimulated) Raman scattering (also downscattering), while the broad features are due to plasmon-to-photon conversion via inverse resonance absorption.

In contrast, the broad $\omega_0/2$ decay features derive from a process which may be termed "inverse resonance absorption." As in resonance absorption, this emission is more efficient for certain plasmon $\mathbf{k}_p$-vectors whose angles with respect to the density gradient coincide with the maximum of the Ginzburg[11] formula for resonance absorption. Since this maximum is not very sharp, and since the perpendicular component of $\mathbf{k}_p$ is directly related to the frequency shift of the plasmon from the center frequency, $\omega_0/2$, we expect broad spectral features whose shifts are sensitive to the density-gradient scale length near $n_c/4$. Indeed, shorter scale lengths produced in high-Z target-irradiation experiments lead to considerably larger displacements to the red and blue of these broad spectral features while affecting the sharp spike only negligibly. It is this effect that has been so disturbing for a long time, since it was in apparent contradiction to the conventional interpretation of these spectra.

In short, the $\omega_0/2$ spectra contain a sharp feature which promises to be a good coronal temperature diagnostic, along with broad features whose dependence on density gradient, temperature, and incident intensity make them all but useless for coronal temperature diagnostics.

Figure 17.22 shows the intensity dependence of the $\omega_0/2$ and $3\omega_0/2$ conversion efficiencies in low-Z CH targets. The differences of 10^4 in the scales are contrary to expectations for upscattering and downscattering (Stokes and anti-Stokes Raman lines), provided the processes happen in the same region in space. However, the latter is

Fig. 17.22
Half-integer harmonic emission from spherical UV-laser CH plasmas. The intensity dependence of the $\omega_0/2$ and $3\omega_0/2$ signals indicated by the shaded curves shows the close relationship between the two harmonics. Both involve plasmons generated by the $2\omega_p$ decay at the $n_c/4$ surface, but the exact generation processes are not just upscattering and downscattering (ordinary Raman Stokes and anti-Stokes lines). The apparent saturation of the signals at high intensities could possibly be due to reduced density scale lengths in the corona of the smaller targets used in this intensity regime.

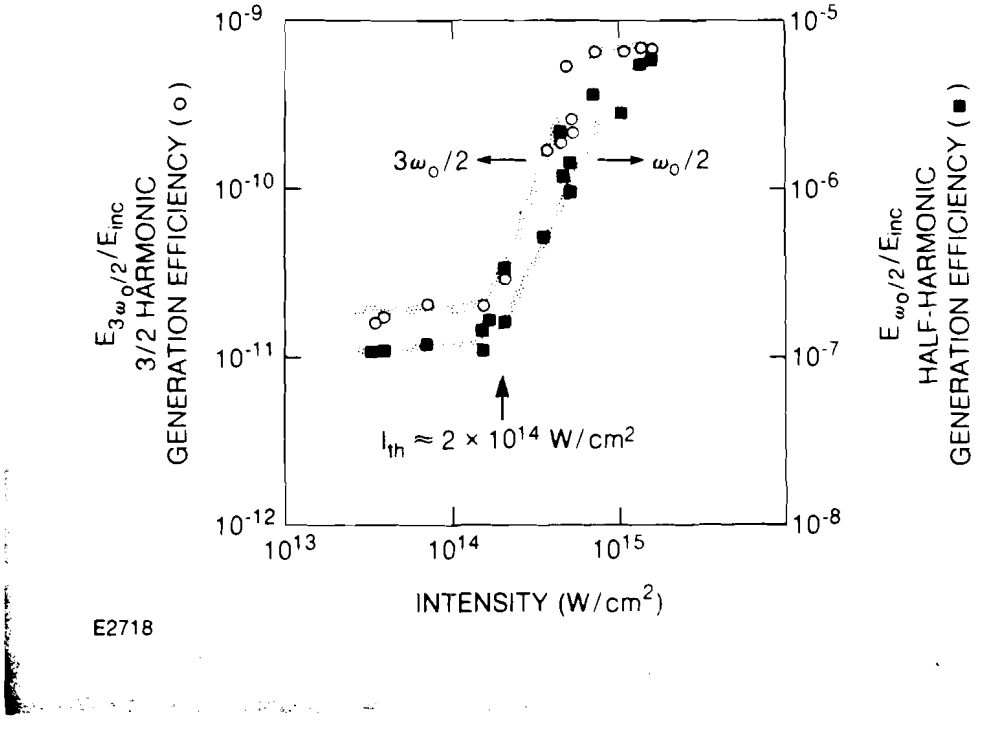

not given *a priori* since detailed analysis of the **k**-vector matching conditions shows that the plasma waves must travel some distance in the density gradient in order to acquire the appropriate **k**-vector length for $3\omega_0/2$ generation.

The two half-harmonics show a clear threshold at ~ 2×10^{14} W/cm^2, in good agreement with the theoretically predicted threshold for the $2\omega_p$ decay instability for our experimental conditions. The close resemblance of the two curves reflects their common element, namely, the plasmons produced by the $2\omega_p$ decay instability. The 3/2 harmonic is produced by the $\mathbf{k}_s = \mathbf{k}_0 + \mathbf{k}_p$, $\omega_s = \omega_0 + \omega_p$ process, and the $\omega_0/2$ harmonic is produced by the downscattering and/or plasmon-photon conversion described earlier. Both curves appear to saturate around 10^{15} W/cm^2. The saturation level for the $\omega_0/2$ generation efficiency is slightly less than 10^{-5}, which is exactly the same saturation level as has been observed in the single-beam experiments in GDL.

High-Z targets show similar generation efficiencies, but the $2\omega_p$ decay threshold is approximately twice that for plastic targets. The shorter scale lengths predicted for these plasmas, along with the slightly higher coronal temperatures, are consistent with this difference.

The similar saturation levels of the half-harmonic conversion efficiency for the single-beam, flat-target experiments and the six-beam, spherical-target experiments are shown in Fig. 17.23. We note a much slower rise for the spherical experiments. This can be explained by assuming spatially uniform illumination and by determining how much of the temporal pulse shape lies above threshold. The

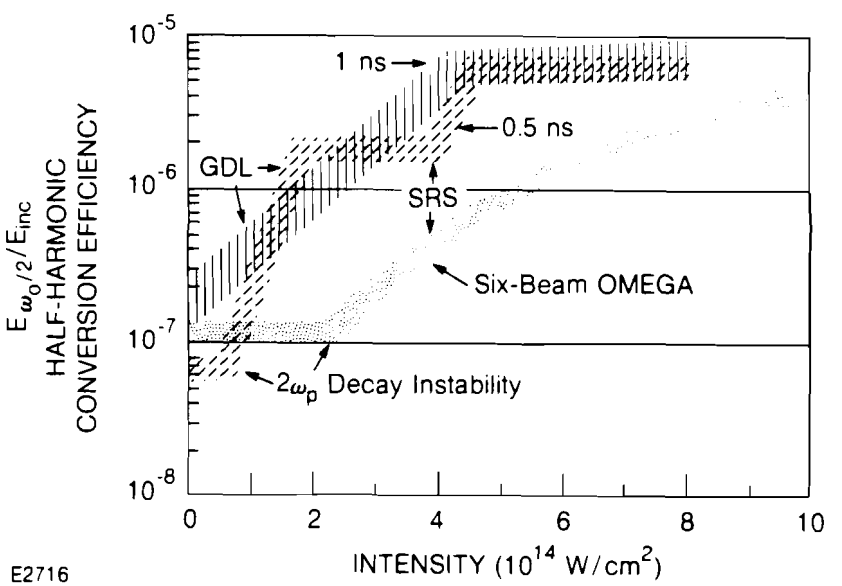

Fig. 17.23
Half-harmonic light emission from spherical and planar UV-laser plasmas using CH targets. We note the increased threshold for the $2\omega_p$ decay instability observed in the spherical irradiation experiments. No separate SRS threshold is observed in either the long-pulse (1-ns) planar plasmas or the spherical experiments.

result is an error-function roughly coinciding with the curve shown in Fig. 17.23. The single-beam experiments, in contrast, are filamentation-driven, leading to a different intensity dependence.

The intensity dependence of the red shift of the sharp $\omega_0/2$ feature (Fig. 17.21) is shown in Fig. 17.24. The circles are for CH targets, and the triangles and square are for Al and Ni targets, respectively. On the right-hand side is a coronal temperature scale related to the wavelength-shift scale according to the relation $\Delta = 31 \times T_{e\,keV}$. The coronal temperatures thus deduced are again somewhat lower than those predicted by hydrocode calculations. Part of this difference may be attributed to the possibility that the sharp spectral feature may be more efficiently radiated early during the pulse, before the $2\omega_p$ decay instability has had time to steepen the density profile near the $n_c/4$ surface. At that time, this feature may become weak, if not extinct. It is certainly worth noting that in Fig. 17.19 we arrived at coronal temperatures between 1.5 and 1.8 keV, quite like the temperatures of ~1.5 keV indicated in Fig. 17.24 that were deduced for the same incident intensity from time-integrated spectra of the type shown in Fig. 17.21.

Fig. 17.24
Coronal electron temperatures as obtained from ordinary Raman-scattering (down-scattering) measurements at $\omega_0/2$ with spherical 650-ps UV illumination. The red shift of the sharp feature of the $\omega_0/2$ spectrum (shown in Fig. 17.21) is shown as a function of incident intensity in OMEGA experiments. The intensity-dependent red shift follows roughly the I law suggested by the shaded area. The red shift, $\Delta\lambda$, is related to the coronal electron temperature by $\Delta\lambda = 31 \times T_{e\,keV}$. The temperatures thus determined lie somewhat below 2-D hydrocode predictions.

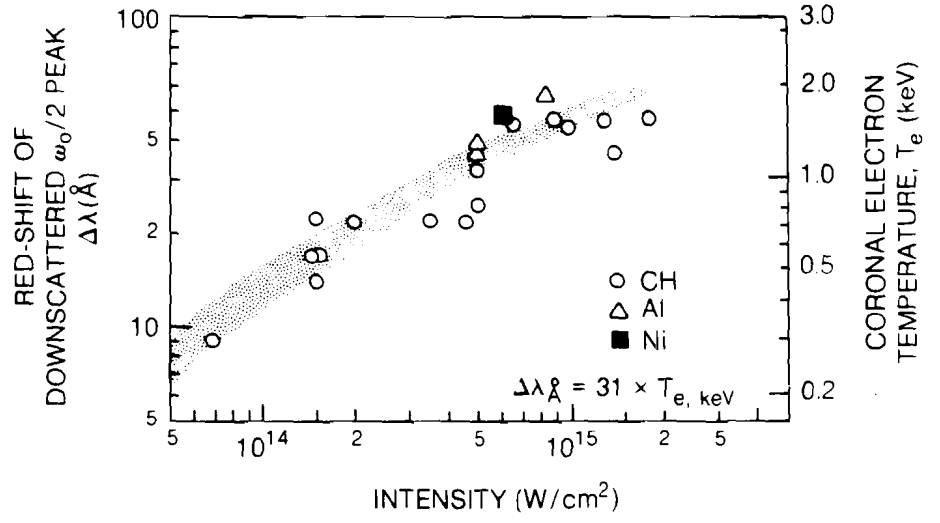

E2724

Figures 17.25 and 17.26 are spectra of the scattered light near the fundamental frequency in backscattering. Figure 17.25 shows the generally narrow backscatter spectra observed in these experiments. The highest-intensity shots under uniform illumination conditions show a weak but discernible red wing which may be attributed to SBS. In contrast, two shots taken at the same irradiation intensity, but for different focusing conditions, show dramatically different spectra as shown in Fig. 17.26. The surface-focus spectra exhibit exactly the same broad spectra seen in single-beam experiments at normal

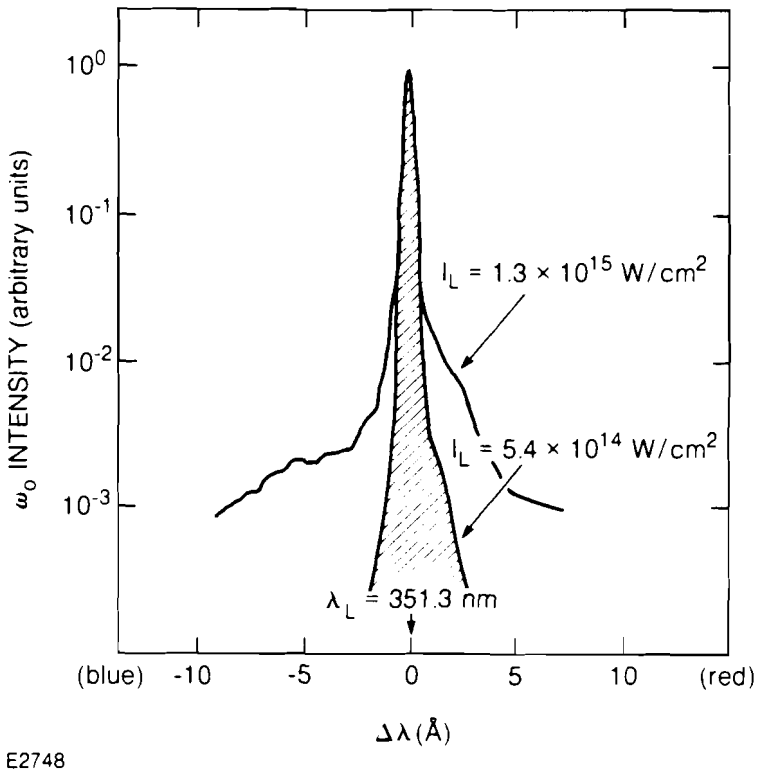

Fig. 17.25
Backscatter spectra at ω_0 from uniformly illuminated (at tangential focus), UV-laser plasmas using spherical CH targets and 0.6-ns pulses. Note the wide dynamic range obtained in these experiments. The principal feature is only Doppler broadened. At the highest accessible intensities, a small, red-shifted SBS component is observed.

incidence. Indeed, the surface-focus experiments may be viewed as six, single-beam experiments at normal incidence. We thus see the dramatic difference between uniform spherical illumination and single-beam experiments. The latter are dominated by self-focusing (filamentation), while the former apparently exhibit a well-behaved 1-D character.

Summary

The OMEGA coronal physics experiments show much-improved coronal plasma conditions, compared to single-beam experiments. Notably, the apparent absence of filamentation of the incident laser light in the corona creates more benign plasma conditions where thresholds for the $2\omega_p$ decay instability now agree with theoretical predictions, and the signatures of this instability, namely the half-harmonic spectra, can now be said to be reasonably understood (3/2-harmonic spectra have not yet been taken). This understanding has enabled us to use one of the $\omega_0/2$ spectral features as a convenient electron-temperature diagnostic. In addition, the presence of very weak SBS radiation has been established at the highest irradiation intensities ($\gtrsim 10^{15}$ W/cm^2) in OMEGA. The high quality of the data and their reproducibility have led to an increased understanding of the plasma physics, while not uncovering any unexpected detrimental effects for direct-drive laser fusion.

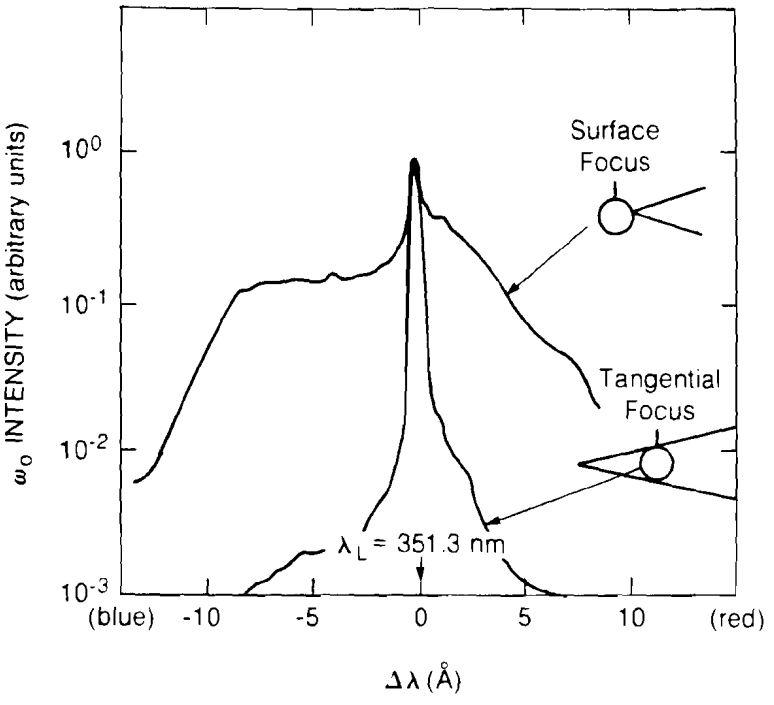

Fig. 17.26
Backscatter spectra at ω_0 from spherical UV-laser plasmas using CH targets and different illumination conditions at constant irradiation intensities (1.3×10^{15} W/cm^2, t_L=0.6 ns). The strongly broadened (red- and blue-shifted) spectra for surface-focused illumination starkly contrast the spectra for tangentially focused, uniform illumination. The former are consistent with earlier single-beam experiments.

ACKNOWLEDGMENT

This work was supported by the U.S. Department of Energy Office of Inertial Fusion under contract number DE-AC08-80DP40124 and by the Laser Fusion Feasibility Project at the Laboratory for Laser Energetics which has the following sponsors: Empire State Electric Energy Research Corporation, General Electric Company, New York State Energy Research and Development Authority, Northeast Utilities Service Company, The Standard Oil Company, and University of Rochester. Such support does not imply endorsement of the content by any of the above parties.

REFERENCES

1. W. Seka, R. S. Craxton, J. Delettrez, L. M. Goldman, R. Keck, R. L. McCrory, D. Shvartz, J. M. Soures, and R. Boni, *Opt. Commun.* **40**, 437 (1982).
2. W. L. Kruer, *Comments Plasma Phys. and Controlled Fusion* 6, 167 (1981); C. E. Max, Lawrence Livermore National Laboratory Report UCRL-53107, 1982; M. N. Rosenbluth, *Phys. Rev. Lett.* **29**, 565 (1972); C. S. Liu in *Advances in Plasma Physics*, edited by A. Simon and W. B. Thompson (Wiley, New York, 1976), Vol. 6, p. 121.
3. R. W. Short, R. Bingham, and E. A. Williams, *Phys. Fluids* **25**, 2302 (1982); R. Bingham and C. N. Lashmore-Davies, *Nucl. Fusion* **16**, 67 (1976); O. Willi and P. T. Rumsby, *Opt. Commun.* **37**, 45 (1981); H. A. Baldis and P. B. Corkum, *Phys. Rev. Lett.* **45**, 1260 (1980).

4. K. Tanaka, L. M. Goldman, W. Seka, R. W. Short, and E. A. Williams, submitted to *Phys. Fluids*.

5. R. W. Short, W. Seka, K. Tanaka, and E. A. Williams, submitted to *Phys. Fluids*; LLE Review **15**, 19 (1983).

6. LLE Review **11**, 3 (1982).

7. LLE Review **14**, 3 (1983); **13**, 18 (1983).

8. K. Tanaka, L. M. Goldman, W. Seka, M. C. Richardson, J. M. Soures, and E. A. Williams, *Phys. Rev. Lett.* **48**, 1179 (1982).

9. W. Seka, E. A. Williams, R. S. Craxton, L. M. Goldman, R. W. Short, and K. Tanaka, submitted to *Phys. Fluids*.

10. A. Simon, R. W. Short, E. A. Williams, and T. Dewandre, submitted to *Phys. Fluids*.

11. V. L. Ginzburg, *The Propagation of Electromagnetic Waves in Plasmas* (Pergamon, New York, 1969).

2.C Thermal Transport and Preheat Measurements with Spherically Illuminated Targets at λ=351 nm

This section describes mass-ablation measurements obtained on OMEGA with six-beam, 351-nm irradiation of spherical targets. Diagnostics used include time-integrated x-ray spectroscopy, charge collectors, plasma calorimetry, and, on some experiments, an x-ray streak camera with a filter array. These data are also used to study the properties of thermal conduction and preheat. We review similar data obtained from 1054-nm spherical irradiation on OMEGA[1,2] and from single-beam, 351-nm irradiation on GDL.[3] These comparisons demonstrate advantages of spherical UV over IR irradiation for laser-fusion applications. As an example, the preheat of inner target layers is lower. The preheat observed in these spherical UV experiments is due to radiation from the high-Z substrate layer in the plastic (CH)-coated targets which is required to generate spectral signatures of the various preheat mechanisms. Since this radiation is not emitted until the heat front arrives at the substrate layer, the preheat can be further reduced by using a sufficiently thick plastic-overcoat layer or by avoiding the use of high-Z materials altogether. This is in contrast to the case of IR illumination where preheat has been shown to be due to hot electrons from the laser-light-absorption region which cannot be significantly attenuated by a plastic coating. Another advantage of UV illumination is that the mass-ablation rate for spherical irradiation is higher by a factor of about 1.5, as compared with spherical IR or flat-target UV irradiation for the same absorbed irradiance. Since absorption of UV light is higher than that of IR light, this factor is higher for comparisons at a fixed incident irradiance, and this factor increases with irradiance.

Previous Experiments at LLE

Figure 17.27 shows a schematic diagram of the targets and a list of the diagnostics used to study thermal transport and mass-ablation rates with six-beam, 351-nm irradiation. The time-integrated spectra

Target Configuration

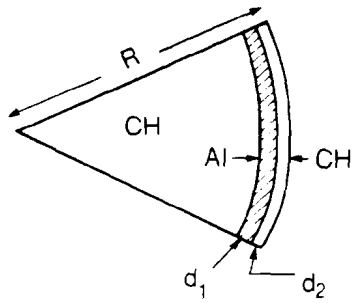

R = 35, 75, or 150 μm
d_1 = 2 μm
d_2 = 0, 2, 4, 6, 8, or 10 μm

E2737

DIAGNOSTICS

Time-Integrated X-Ray Spectroscopy
Charged Particle Detectors
Plasma Calorimetry

LASER

Six Beams
λ = 351 nm
Pulse Width: 600 ps
Irradiance: 10^{14}, 5×10^{14}, 10^{15} W/cm^2
Energy: 150-235 J

Fig. 17.27
Targets for transport "burn-through" measurements on 351-nm illuminated, uniformly irradiated spherical targets. Radiation from the Al substrate layer signals the arrival of the heat front. Other substrate materials are also used.

obtained in these studies also provide a measure of preheat as determined by K_α lines. The figure also lists the laser parameters. An x-ray streak camera with a filter array was used on some of the experiments, and these results are described below. The targets were chosen to be solid spheres so that transport and mass ablation could be studied independently of implosion and stability effects.

We first summarize the main conclusions of previous thermal-transport studies at LLE, which will be compared later with the results of new experiments with six UV beams. Experiments using a single UV beam to irradiate a plane target give "burn-through" results that agree with the predictions of a flux-limited transport model with a flux-limit parameter of f=0.03.[3] The transport measurements using 1054-nm spherical irradiation[1,2] show that the heat-front penetration, or burn-through, is about three times deeper than for non-spherical irradiation and deeper by about the same factor than the penetration predicted by the *LILAC* code for spherical irradiation and a similar flux-limited transport model. The penetration of the heat front, as measured by K lines of the high-Z substrate (Ti or Ni), is smaller by about a factor of 2 than that measured by Al K lines. Since the former lines appear at higher temperatures (1 keV and 1.5 keV, respectively) than the latter (~ 400 eV), these results imply a moderate temperature gradient at the heat front, as compared with the steep temperature profiles predicted by a flux-limited model.

These earlier experiments show that the spectroscopic determinations of ablation rates give higher values than those deduced by charge collectors. The spectroscopic diagnostics include crystal spectrographs and x-ray streak cameras. Charge-collector measurements give the ablated mass from the known absorbed energy and the expansion-velocity spectrum. The mass-ablation rate $\dot{m}$ deduced

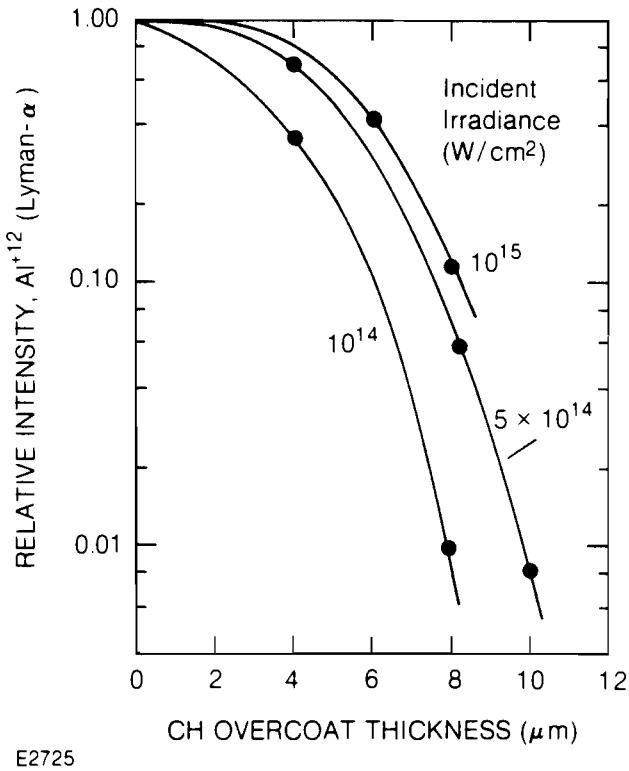

Fig. 17.28
Thermal-transport burn-through measurements using six-beam, 351-nm irradiation and CH-coated Al-substrate targets. The mass-ablation rate may be estimated by dividing the burn-through depth by the laser pulse width.

from charge collectors can be considered a lower bound, because partially ionized material is not fully weighted by charge-collector currents and is always measured to be slower than fully ionized material. These earlier experiments are described in more detail in LLE Review, Volume 13.[1]

New Burn-Through Measurements

Figures 17.28 and 17.29 show the burn-through curves obtained in the present six-beam UV experiments. Figure 17.28 gives burn-through results for plastic-coated aluminum targets, and in Fig. 17.29, aluminum is replaced by titanium. The observed spectral line intensities are plotted as functions of the plastic-coating thickness. Each curve pertains to a given irradiance at a fixed 600-ps pulse width. Each curve is separately normalized. The fall-off in intensity with increasing coating thickness shows the maximum penetration of the heat front in plastic for the given laser pulse. Since spectral line emission occurs at different temperatures, depending on the substrate material and on the chosen spectral line, such burn-through data can indicate the shape of the temperature profile of the heat front. Figure 17.30 shows the corresponding burn-through curves calculated by *LILAC* for the case of plastic-coated aluminum. The right-hand border of each band corresponds to a flux-limit parameter f=0.1, and the left-hand border corresponds to f=0.04. For an irradiance of 10^{14} W/cm^2, the two curves essentially coincide.

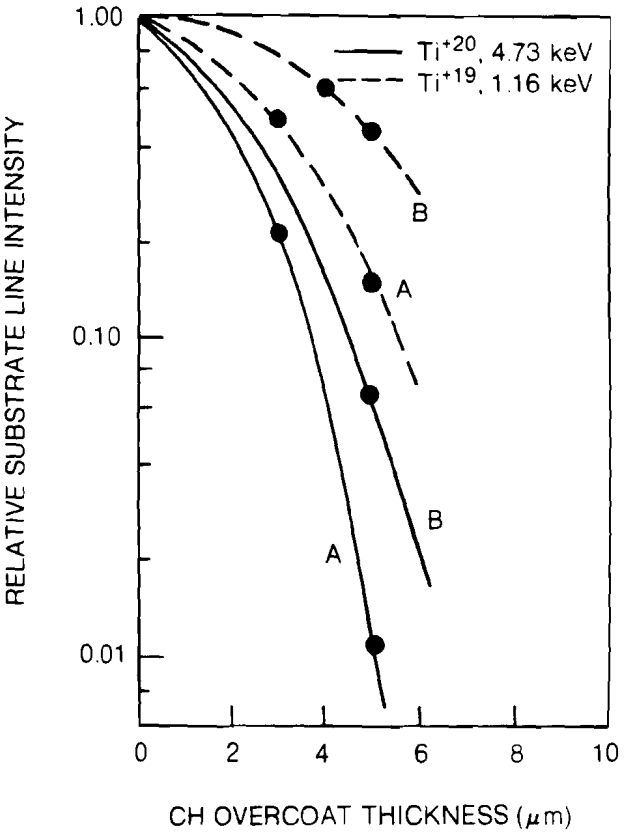

Fig. 17.29
Transport measurement in CH-coated Ti-substrate targets using six-beam, 351-nm irradiation at (a) 10^{14} W/cm^2 and (b) 5×10^{14} W/cm^2. Since the characteristic line emission of the two ion species considered is emitted at different temperatures, the difference in burn-through depths obtained for each species with a given pulse gives an indication of the scale length of the temperature profile of the heat front.

The results for 351-nm spherical irradiation are generally similar to those obtained for 1054-nm spherical irradiation. The heat front is less steep than predicted by a flux-limited model. This is evidenced by:

(a) more gradual fall-off of these curves, as compared with the predicted curves in Fig. 17.30.

(b) deeper penetration for aluminum K lines (Fig. 17.28), as compared with titanium K lines (Fig. 17.29).

(c) deeper penetration of titanium L lines (Ti^{+19}, 2p-5d transitions) as compared with titanium K lines (Ti^{+20}, $1s^2$-1s2p).

The lower-energy lines of Al^{+12} and Ti^{+19} ions generally show deeper penetration than predicted by *LILAC*. By comparing Fig. 17.28 and Fig. 17.30, we observe that the progression of penetration depth with irradiance is much slower than predicted by the code. At the irradiances of 10^{14}, 5×10^{14}, and 10^{15} W/cm^2, the measured penetration depth is larger than predicted by about a factor of 3, 2, and 1.5, respectively. With 1054-nm irradiation, this ratio is approximately 2 for the range of irradiance 5×10^{13} to 10^{15} W/cm^2.

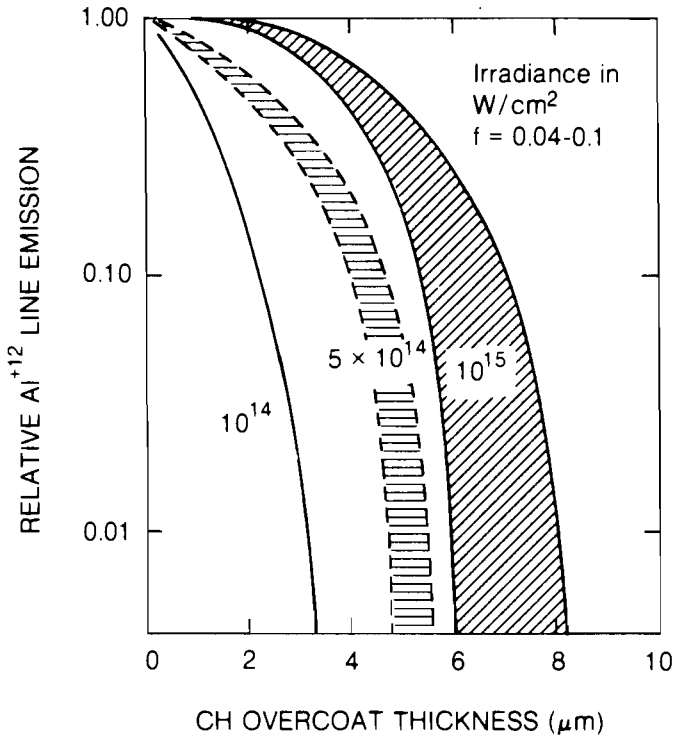

Fig. 17.30
LILAC-*calculated burn-through curves for CH-coated Al-substrate targets. The width of each band corresponds to the flux-limit-parameter range 0.04 to 0.1.*

It is important to note that the measured burn-through is deeper than that calculated for flux-limit parameter values in the range of 0.04-0.1 and that, in fact, the results cannot be explained by any value of f, especially for the lower irradiances. We have tentatively attributed these deep-penetration results to effects of long-mean-free-path (mfp) electrons, or non-local thermal transport. It is not very surprising to observe similar non-local transport effects at the two wavelengths. The importance of non-local effects to a burn-through rate has been shown to depend on the factor by which the electron mfp exceeds the temperature scale length.[4] Even though the electron mfp is shorter for UV irradiation because of the higher density in the laser-matter interaction zone, the temperature scale length in the target is also shorter at this shorter wavelength, and the mfp/scale-length ratio should not change appreciably with wavelength.

Mass-Ablation-Rate Measurements

Mass-ablation rates can be deduced from the total ablated mass, defined conservatively as the thickness which causes the substrate x-ray emission to drop by a factor of 10. After dividing the ablated mass by the laser pulse width (FWHM), we multiply by a correction factor (equal to 0.78) which relates the peak mass-ablation rate to the total ablated mass divided by the pulse width.[5] The results obtained from the aluminum data of Fig. 17.28 are shown at the top of

Fig. 17.31. This figure also shows planar-target burn-through results at 351 nm and spherical-target results at 1054 nm obtained using time-integrated and time-resolved (streak) spectral data and charge-collector data. These earlier results, including results obtained at the Rutherford Laboratory,[6] are discussed in LLE Review, Volume 13.[1]

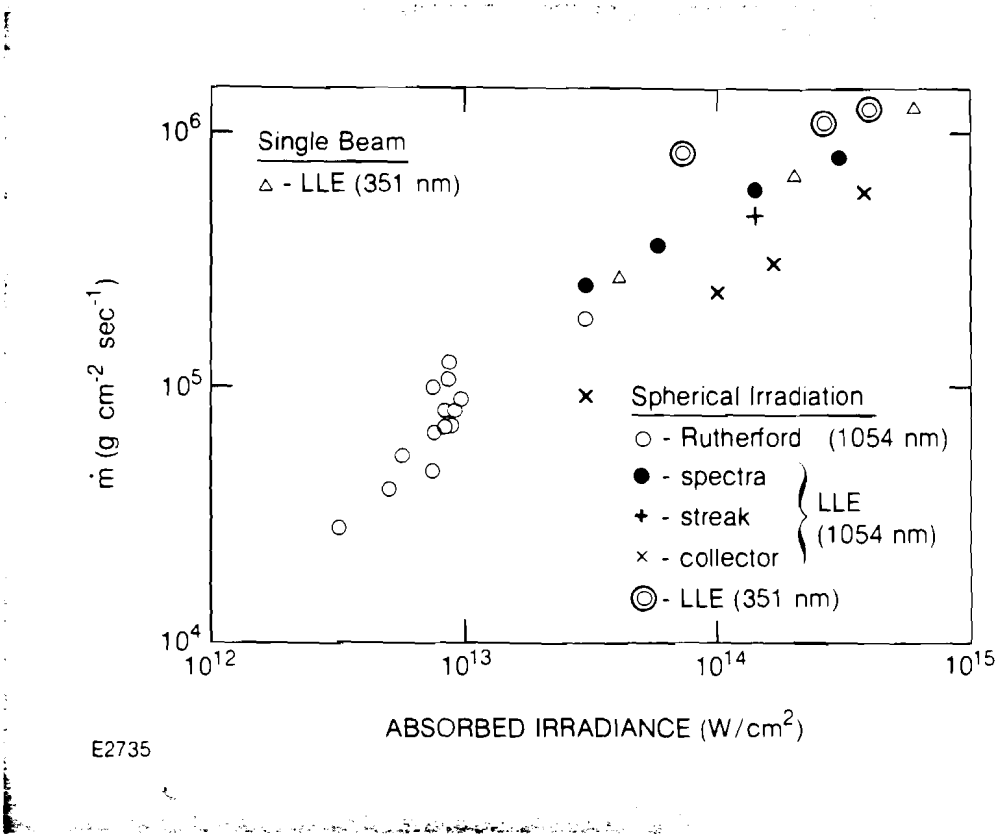

Fig. 17.31
Comparative mass-ablation rates for coated aluminum targets. Rates are obtained from spectral burn-through data and from other diagnostics. Among the new 351-nm data are data points from 1053-nm experiments performed at LLE and at the Rutherford Laboratory.[6]

The mass-ablation rates for spherical UV irradiation are higher than for either IR spherical or single-beam UV irradiation. This comparison is made for the same type of measurement in all three cases, namely, burn-through curves using the Al^{+12} Lyman-α line (1.728 keV). It should be emphasized that the comparison here and in subsequent figures is for the same absorbed irradiance. Obviously, this advantage of UV irradiation is in addition to the advantage of higher absorption; if the same comparison is made for the same incident irradiation, the advantage of UV is even more apparent.

An alternative way of determining the mass-ablation rate is by using charge-collector data which show a distinct and narrow velocity spectrum of the expanding plasma. Through this spectrum and the known absorbed energy, we derive the mass-ablation rate shown in Fig. 17.32. Again, if we compare results in UV and IR obtained in the same way (charge collectors), the rate is decidedly higher in UV than in IR. Since $\dot{m}$ is approximately given by the ratio of the absorbed irradiance and the square of the plasma velocity, this result can be stated differently: for a given absorbed irradiance, the expansion velocity is lower in UV than in IR. Indeed, the velocity corresponding to the current peak was found to follow the following

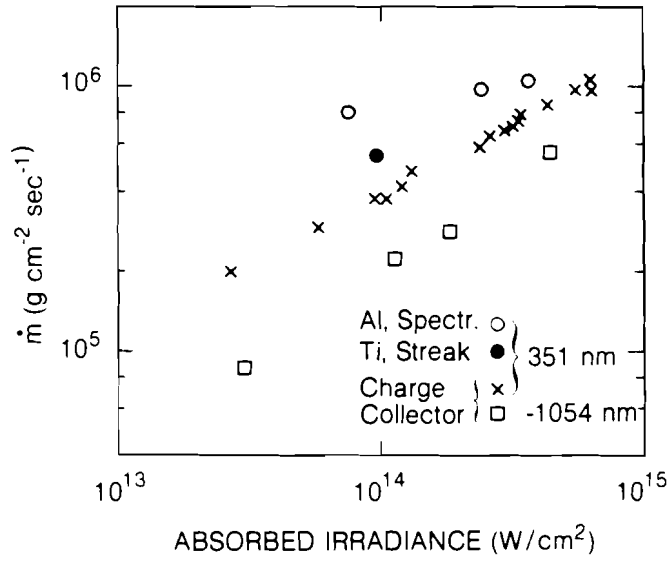

Fig. 17.32
Comparative mass-ablation rates obtained from spherical irradiation experiments. Results using various diagnostics and both aluminum and titanium substrates are compared.

scaling: $v_p = 6.9 \times 10^7\ I^{0.15}$ in UV and $v_p = 8.7 \times 10^7\ I^{0.15}$ in IR. Here, v_p is in cm/sec, and I is the absorbed irradiance in units of 10^{14} W/cm^2.

The x-ray streak camera determines $\dot{m}$ by measuring the onset time of K radiation from metal-substrate targets with various thicknesses of plastic overcoat, thus measuring the time required to ablate away a known mass of plastic. The results (Fig. 17.32) for titanium substrates are intermediate to those obtained from charge collectors and those obtained from Al^{+12} spectra. This result is consistent with spectroscopic burn-through results where titanium K radiation also indicates less penetration than does aluminum radiation (see Figs. 17.28 and 17.29).

From the mass-ablation rate, we derive the ablation pressure. The relationship usually employed is $P=\dot{m}\langle v\rangle$, where $\langle v\rangle$ is the mean expansion velocity. This relationship can only be expected to be precise to within a factor of order 1, and, indeed, code simulations show that a correction factor must be applied which lowers the pressure thus calculated by about 30%. It should be emphasized that this correction factor simply reflects internal consistency between calculating pressure through the equation of momentum conservation and the actual peak ablation pressure; the question of the correctness of the transport description in the code is of second order in importance. To be conservative, we used the $\dot{m}$ results derived from charge-collector data, which are lower than those derived from x-ray spectra. These results are shown in Fig. 17.33, compared with *LILAC* calculations for two flux-limiter values, 0.04 and 0.1. The agreement is very good. We note, incidentally, that such comparisons (and those based on streak-camera data) are not nearly as good for deducing f

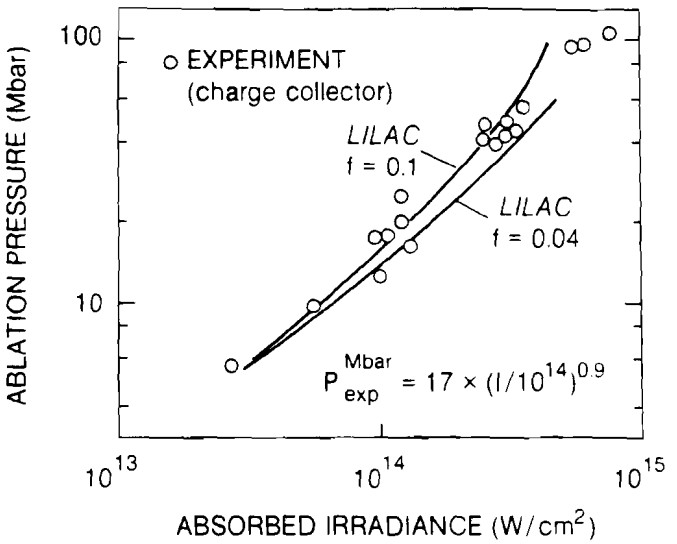

Fig 17.33
Ablation pressure in six-beam, 351-nm irradiation. Simulation results from LILAC *show good agreement over a range of flux-limit parameters.*

values as those based on burn-through curves, because the simulation results for a broad range of relevant f values fall within the scatter of the ablation-rate measurements. On the other hand, even with very large errors in measuring the intensity of the K-line radiation, the position of the steeply falling portion of the burn-through curve, and, thus, the IR penetration depth, will not be seriously in error. The precision in the abscissa (plastic thickness) is, of course, very high.

Preheat Measurements

Information on preheat can be obtained by the observation of the K_α line from cold titanium for various thicknesses of CH overcoating. For comparison, we show in Fig. 17.34 spectra obtained with 1054-nm spherical irradiation and the corresponding 351-nm data in the following figure (Fig. 17.35). The interesting thing to note in Fig. 17.34 is that in IR irradiation, the Ti^{+20} lines (coming from the hot plasma or the heat front) decay rapidly with increasing CH thickness, whereas the K_α line, which is very weak, persists in much thicker CH layers. In going from 2- to 6-μm CH thickness, the K_α line goes down in intensity by only a factor of 1.5, whereas the Ti^{+20} goes down by a factor of about 100. This occurs because the range of the fast electrons from the laser-interaction region is longer than the heat-front scale length, which allows the electrons to excite the K_α line ahead of the heat front. By comparison, Fig. 17.35 shows that with UV irradiation, the Ti^{+20} and K_α lines go down in almost exactly the same proportion as the CH thickness increases. This is a strong indication that K_α is excited by radiation emitted from the substrate as the heat-front arrives at the substrate, rather than by hot or "fast" electrons preceding the heat front. The absolute intensity of the K_α line in Fig. 17.35 is about 60

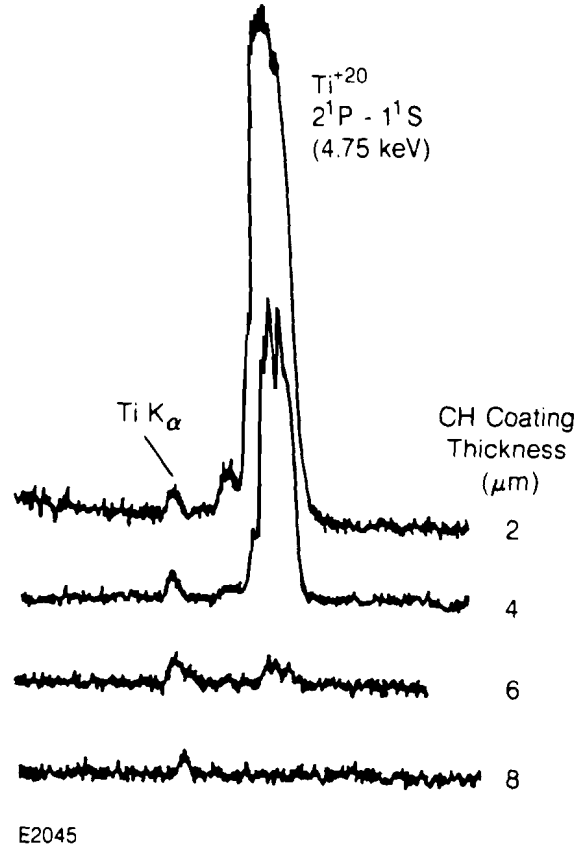

Fig. 17.34
Preheat measurement using 1054-nm irradiation and CH-coated titanium shells. The Ti^{+20} line decreases with increasing CH-layer thickness much faster than the Ti K_α radiation which persists to greater depths due to the long-range penetration of hot electrons into the cold substrate.

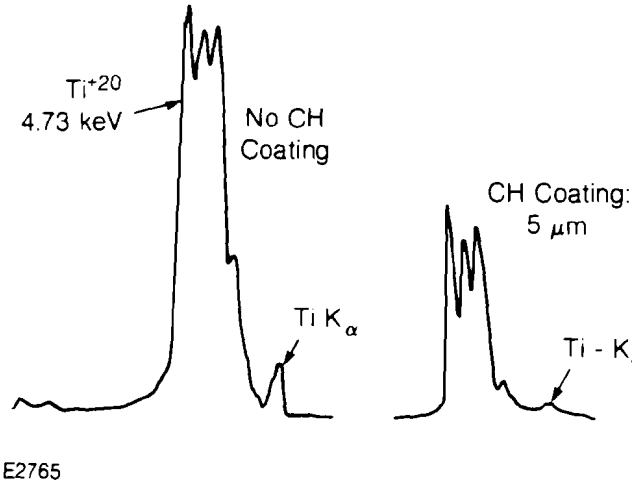

Fig. 17.35
Radiative preheat in six-beam, 351-nm irradiation. The K_α radiation is seen to decrease with increased CH coating thickness at the same rate as the Ti^{+20} lines. This suggests that the K_α radiation from colder substrate material is excited by radiation from the heated surface of the substrate.

times weaker than the Ti^{+20} resonance line, indicating only a few percent of the absorbed energy going into preheat. The important inference from these measurements is that for the UV illumination of a CH layer in the range of intensities considered, there is no measurable long-range preheat as with IR illumination. Furthermore, with CH coatings over high-Z substrates where the coating thickness is greater than the thermal penetration depth, the level of radiative preheat is extremely low.

We show in Fig. 17.36 the observed K_α intensity data plotted as a function of CH coating thickness over various substrate materials for 4×10^{14} W/cm^2 and for 1054-nm and 352-nm irradiation. The curves give theoretical predictions of the decay of electron-excited K_α intensity with increasing coating thickness, based on the expected attenuation of the hot-electron flux through the given thicknesses of plastic, for various values of the hot-electron temperature T_H. The comparison of targets with and without plastic coatings is meaningful, since the laser-energy absorption efficiency in plastic and in titanium for this irradiance is very nearly the same (50-60%), and since the dependence of T_H on the target Z is very weak. If preheat were produced by fast electrons in the UV experiment (as indeed it is in the IR experiment), the observed decay rate would correspond to the extremely low T_H value of 3 keV. The range of these hot electrons would be nearly the same as the heat-front scale length (indicated by Fig. 17.29). In this case, the hot electrons could not penetrate into the cooler, un-ionized substrate material ahead of the heat front, and there would be no possibility for K_α emission. This again supports the

Fig. 17.36
K_α measurement of the fast-electron temperature T_H using spherical 1054- and 351-nm illumination at 4×10^{14} W/cm^2. The points show the observed decay of K_α intensity with increasingly thick CH coatings. Theoretical curves for this decay at different T_H values suggest too low a T_H value for the 351-nm results to cause electron-excited K_α emission in advance of the heat front. All data and curves are normalized to unit intensity at zero coating thickness.

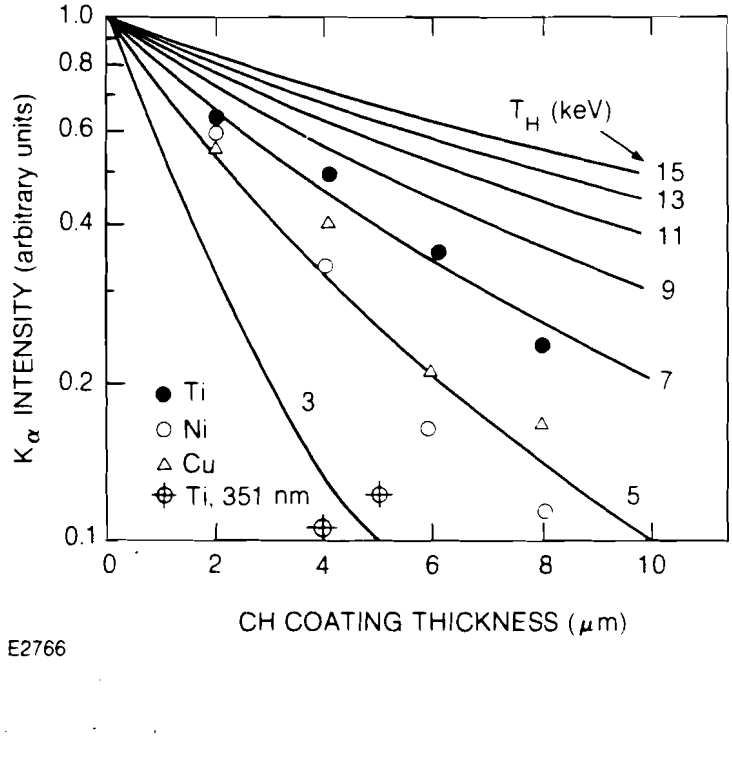

conclusion that what little preheat is indicated in Fig. 17.35 is due to titanium radiation and not due to longer-range hot electrons generated in the laser-interaction region.

Summary

Mass-ablation rates obtained with spherical UV irradiation are higher than those obtained with spherical IR irradiation at the same absorbed irradiance by a factor which varies with irradiance from 1.5 to 2.0. When this comparison is made on the basis of incident irradiance, the advantage of UV is considerably greater. The fact that mass-ablation rates derived from x-ray spectroscopic results are higher than those derived from charge-collectors suggests that complex theoretical and experimental issues in thermal-transport physics remain to be solved. Ablation pressures derived from the (more conservative) mass-ablation rates obtained from charge-collector data are consistent with numerical simulation results. The preheat levels measured by K_α emission from plastic-coated titanium targets show that the K_α line is excited primarily by x-ray radiation from the titanium and that preheat levels obtained with UV irradiation on sufficiently thick plastic coatings are less than 1% of the absorbed energy.

ACKNOWLEDGMENT

This work was supported by the U.S. Department of Energy Office of Inertial Fusion under contract number DE-AC08-80DP40124 and by the Laser Fusion Feasibility Project at the Laboratory for Laser Energetics which has the following sponsors: Empire State Electric Energy Research Corporation, General Electric Company, New York State Energy Research and Development Authority, Northeast Utilities Service Company, The Standard Oil Company, and University of Rochester. Such support does not imply endorsement of the content by any of the above parties.

REFERENCES

1. LLE Review **13**, 12 (1982).
2. B. Yaakobi, J. Delettrez, L. M. Goldman, R. L. McCrory, R. Marjoribanks, M. C. Richardson, D. Shvartz, S. Skupsky, J. M. Soures, C. Verdon, D. M. Villeneuve, T. Boehly, R. Hutchison, and S. Letzring, *Phys. Fluids* (accepted for publication).
3. B. Yaakobi, T. Boehly, P. Bourke, Y. Conturie, R. S. Craxton, J. Delettrez, J. M. Forsyth, R. D. Frankel, L. M. Goldman, R. L. McCrory, M. C. Richardson, W. Seka, D. Shvarts, and J. M. Soures, *Opt. Commun.* **39**, 175 (1981).
4. LLE Review 7, 20 (1981).
5. Rutherford Laboratory Annual Report RL-81-040, Chap. 4.4 (1981).
6. T. J. Goldsack *et al.*, *Phys. Fluids* **25**, 1634 (1982).

Section 3
ADVANCED TECHNOLOGY DEVELOPMENTS

3.A Time-Resolved, Laser-Induced Phase Transition in Aluminum

Phase transformation in condensed matter is an important area of study in solid-state physics and material science, since it relates to the microstructural evolution of matter, yet the mechanism and time history of such a transformation is still not known. Several theories have been proposed to describe this phenomenon, but serious flaws are evident in all of them. A basic problem has been the lack of experimental information upon which to base a model. The laser has become a valuable tool in the study of melting processes in the past few years. However, only indirect inferences have been obtained concerning any time-resolved structural evolution, since the probes have measured changes in surface reflection,[1,2] surface second-harmonic generation,[3] electrical conductivity,[4] and lattice strain[5] during laser-induced phase transitions.

Recently, a technique has been developed and implemented at LLE that enables laser-induced order-disorder transformations to be directly monitored on the picosecond timescale.[6] The technique is based upon observing the electron diffraction pattern of the phase of the system under study. By using a short pulse of monoenergetic electrons to probe a thin specimen, it is now possible to take a snapshot of the system's ordered (or disordered) structure. The duration of the electron pulse is ~30 ps. Synchronized to this electron pulse is a laser pulse which is used to stimulate the phase transition (i.e., melt the solid). By probing the sample with the electron pulse at known times after the laser stimulus, information can be obtained on the evolution of the melting process.

For example, the actual time required for a given system to undergo a laser-induced phase transformation can now be determined. Conflicting theories placed this number between a few picoseconds,[7] where the cloud of laser-generated hot electrons rapidly transfers energy to the lattice, and the lattice dissolves; and >200 ns,[8] where the lattice only "softens" due to the increased temperature, and the ions remain relatively stationary. The picosecond electron-diffraction technique is well-suited for taking this measurement.

The Experiment

The experimental arrangement used to time-resolve the phase transformation is shown in Fig. 17.37. The electron-pulse generator is a modified streak camera tube. In its normal configuration, this tube is a diagnostic tool capable of time-resolving short optical pulses. The tube converts an optical pulse to an electron pulse through the photoelectric effect while preserving the temporal profile of the pulse. The electrons are then accelerated and deflected or "streaked" to map the temporal information of the pulse across the phosphor screen. The key features of this tube are the following: (1) It is capable of generating short electron bursts down to single-picosecond durations. (2) The electrons are monoenergetic to one part in 10^4. (3) The electron pulse can be synchronized to the original optical pulse with picosecond accuracy. For the purpose of this experiment, the deflection plates are of no use and have been removed. The remaining components are the photocathode, grid, focus cone, and anode. Once generated, the electron pulse accelerates through the tube to the anode and then "drifts" at a constant velocity $\sim 10^8$ m/s. The specimen to be studied is positioned in this drift region. The electron pulse passes through the specimen (aluminum in this case) that is of a proper thickness ($\sim$ 240 Å) such that each electron in the pulse sustains, on the average, one elastic collision. The aluminum films were made by first depositing aluminum onto a Formvar substrate and then vapor-etching to dissolve the Formvar. The singly scattered (diffracted) electrons then travel to the phosphor screen where they are visualized. The diffraction ring pattern produced, shown in Fig. 17.38(a), is a result of the wave-like properties of the electrons and the ordered polycrystalline nature of the aluminum specimen. By careful measurement of the ring diameters and by use of the Bragg relation, the lattice constant for the crystal is determined to be 4.03±0.08 Å, in close agreement with the known value of 4.05 Å.

The signal-to-noise ratio of the pattern is rather low, due to the low electron flux required to maintain a 30-ps pulse width. Increasing the electron flux causes space-charge broadening to occur, which stretches the pulse duration. To make the best possible use of the available signal, circular signal averaging about the center of the diffraction pattern is performed. Circular averaging smooths the randomly generated noise to a roughly constant background level, thus greatly enhancing the signal-to-noise ratio. Figure 17.38(b) shows the result of circular averaging, which is accomplished by simply spinning a photograph of the diffraction pattern.

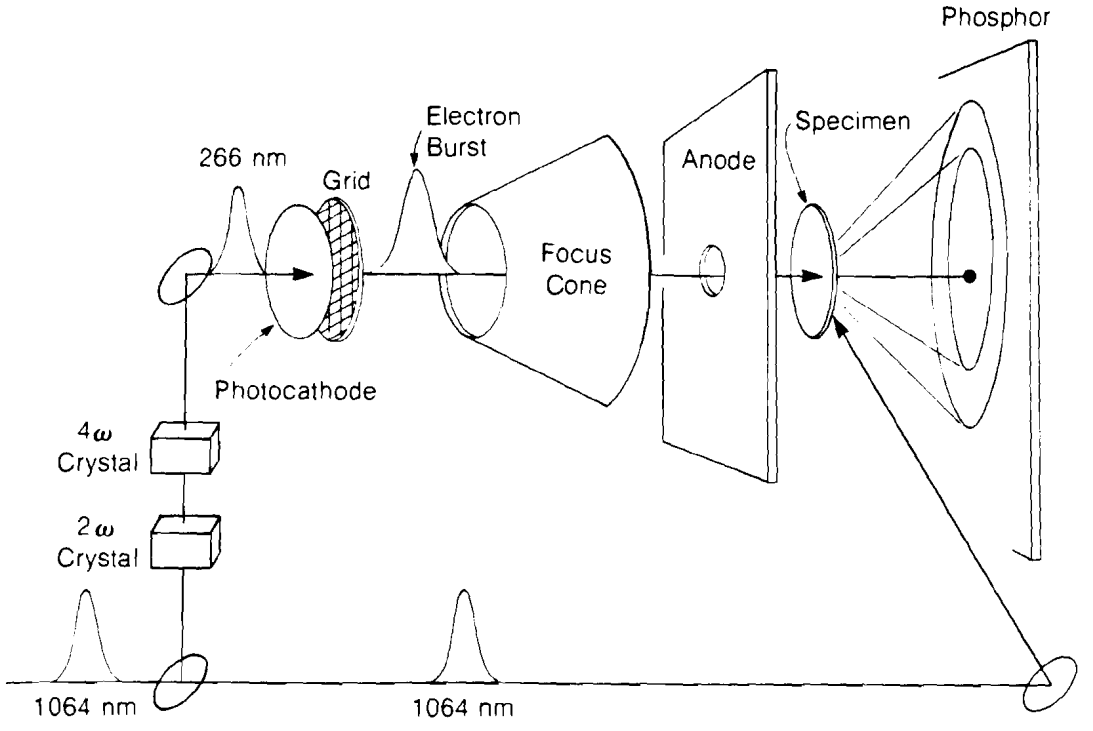

Fig. 17.37
Experimental layout for monitoring the laser-induced phase transition occurring in aluminum. The electron-pulse generator is comprised of a photocathode (at -25 kV), grid, focus cone, and anode (at ground potential). The specimen is located in the path of the electron beam. A variable-delay arm was placed in the 1064-nm beam in order to allow for laser-stimulus/electron-probe synchronization.

It is important that the laser stimulus be uniform in space over the probed region of the specimen. Therefore, the laser-beam diameter was expanded to ~6 mm to overfill the 2-mm specimen diameter, and the electron-probe diameter was reduced to ~1 mm. In this configuration, the probed region of the aluminum has a variation in fluence from the stimulus of no more than 15% from center to edge. The absorption of the laser stimulus (λ=1064 nm) by the specimens is 13 ±1%.

Synchronization between the laser stimulus and the probe pulse is accomplished by means of a laser-activated electron-deflection technique.[9] A fast deflection-plate assembly through which the electron pulse travels is positioned in place of the specimen. A photoconductive switch, activated with picosecond accuracy by the laser stimulus, charges the plates, establishing an electric field in a time on the order of the laser-pulse duration (~ 30 ps). If the laser stimulus arrives early, relative to the electron pulse, the electrons deflected by the electric field are detected at a new position on the phosphor screen. Proper synchronization between the two pulses is achieved when the electron pulse is evenly streaked between the undeflected and fully deflected positions on the phosphor screen.

The procedure followed is to irradiate the specimen with the laser stimulus and, at various times thereafter, to probe the structure of the aluminum with the electrons. This process was repeated at several laser-pulse energy levels. Figure 17.39 displays two diffraction patterns of the same aluminum specimen (a) before and (b) during the laser-induced melt phase. The most distinct difference between the two figures is seen in the nearly complete loss of intensity of the two outer rings in Fig. 17.39(b). In this case, the ordered structure has been degraded as a consequence of the formation of a liquid phase. The specimens were used only once, although at fluence levels of 7-10 mJ/cm^2, the specimens frequently survived multiple shots.

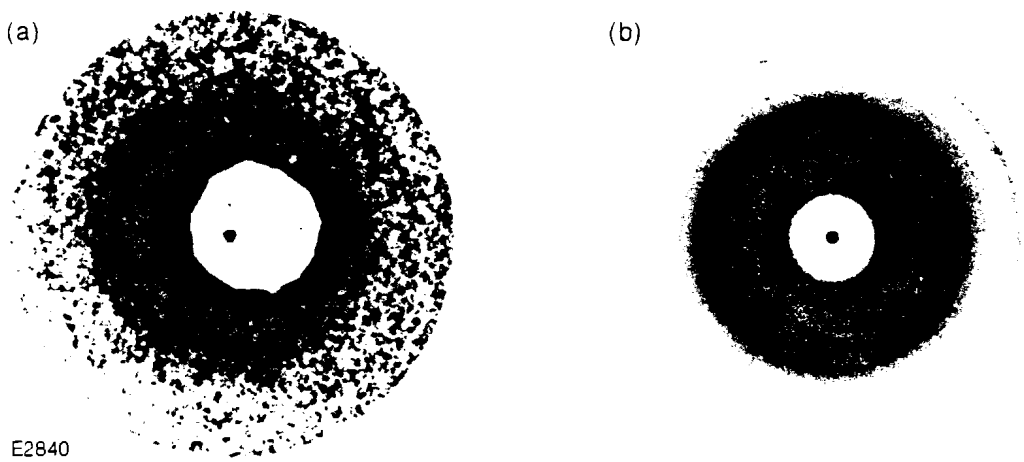

Fig. 17.38
(a) Photograph of the diffraction pattern of a 240-Å-thick film of aluminum as seen on image intensifier. The dark mask at the center (#96 wratten filter) acts to block the intense zero-order mode of the diffraction pattern. Only the intense center spot transmits through to the film.
(b) The center of the rings is the zero-order spot. Rotating the image about this point results in an appreciable enhancement in the signal-to-noise ratio. The background noise is smoothed to a constant background level, causing the rings to stand out more clearly.

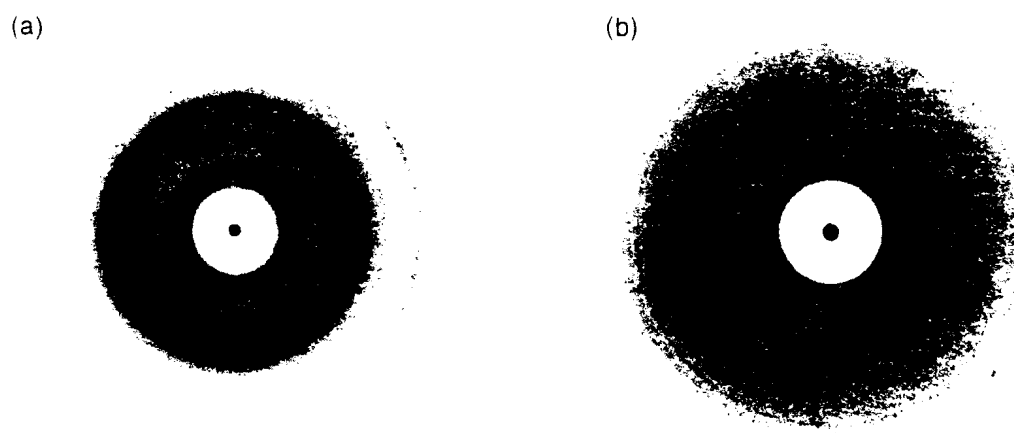

Fig. 17.39
(a) A diffraction pattern of aluminum prior to the arrival of the laser stimulus.
(b) The same specimen as used in (a), but in the liquid phase. The electron probe follows the laser stimulus by 1 ns.

Figure 17.40 shows the results of this preliminary experiment. The curve represents the fluence required to transform the aluminum specimen from the solid to the liquid phase at a given delay time. We see that the curve falls exponentially to an asymptotic value corresponding to the latent heat of the liquid state. At short delay times (<20 ps), the curve becomes indistinct due to the limited temporal resolution of the probe.

Though the actual phase transition has not been time-resolved, it clearly occurs on a timescale shorter than 20 ps. The fact that an increase in fluence is required to cause the phase transition for short delays (~ 100 ps) implies that for lower fluences at such delays, the specimen must be in a super-heated solid state.

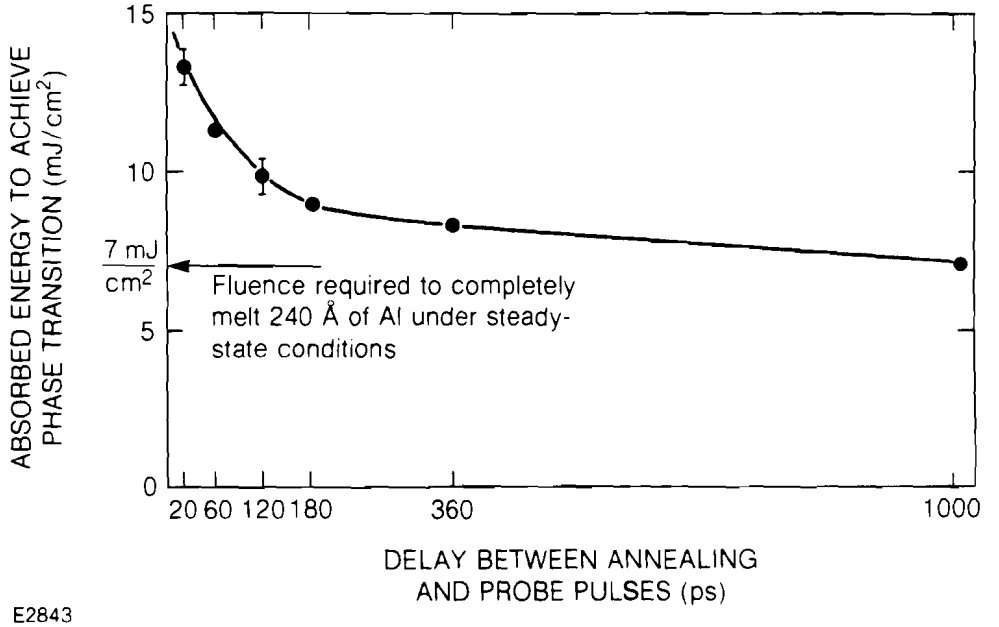

Fig. 17.40
This plot shows the absorbed energy per unit area required to achieve a phase transition after a given delay time. The error bars span the two discrete stimulus levels used that were found to be immediately above and below the level required to cause the phase transition at the indicated time delay.

Summary

We have demonstrated an application of the picosecond electron-diffraction technique by resolving the delay between the laser stimulus of a polycrystalline solid and the moment the melt occurs. True time resolution of the solid-liquid transition will require that the probe duration be much shorter, perhaps down to the single-picosecond timescale. With the present system, however, a great deal of information can be collected about laser-induced phase transitions. In addition to monitoring changes in phase, the electrons, under optimal conditions, can measure the change in the lattice constant resulting from an increase in temperature. This information will become most valuable in determining how far the melt temperature is exceeded before the system collapses into the liquid (or vapor) phase.

ACKNOWLEDGMENT

This work was supported by the following sponsors of the Laser Fusion Feasibility Project at the Laboratory for Laser Energetics—Empire State Electric Energy Research Corporation, General Electric Company, New York State Energy Research and Development Authority, Northeast Utilities Service Company, The Standard Oil Company, and University of Rochester. Such support does not imply endorsement of the content by any of the above parties.

REFERENCES

1. D. H. Lowndes and R. F. Wood, *Appl. Phys. Lett.* **38**, 971 (1981).
2. G. L. Olson, S. A. Kokorowski, R. A. McFarlane, and L. D. Hess, *Appl. Phys. Lett.* **37**, 1019 (1980).
3. C. V. Shank, R. Yen, and C. Hirlimann, *Phys. Rev. Lett.* **50**, 454 (1983).
4. G. J. Galvin *et al.*, *Phys. Rev. Lett.* **48**, 33 (1981).
5. B. C. Larson, C. W. White, T. S. Noggle, and D. Mills, *Phys. Rev. Lett.* **48**, 337 (1982).
6. G. Mourou and S. Williamson, *Appl. Phys. Lett.* **41**, 44 (1982).
7. R. F. Wood and G. E. Giles, *Phys. Rev. B* **23**, 2923 (1981).
8. J. A. Van Vechten and M. Wautelet, *Phys. Rev. B* **23**, 5543 (1981).
9. LLE Review **16**, 54 (1983).

Section 4
NATIONAL LASER USERS FACILITY NEWS

This report covers the activities of the National Laser Users Facility (NLUF) during the quarter 1 October to 31 December 1983. During this period, three users conducted experiments on LLE facilities. Visiting scientists representing the University of Connecticut and the University of Pennsylvania conducted experiments on the Glass Development Laser (GDL), compiling a total of 39 shots. An additional group representing the University of Maryland, the Naval Research Laboratory, and the Goddard Space Flight Center conducted experiments on the OMEGA facility, compiling a total of 25 shots. A specific listing of shots can be found in Section 1 (LASER SYSTEM REPORT) of this issue.

The two user experiments on the GDL system used 351-nm laser light focused onto flat targets for x-ray diffraction experiments. The participating individuals of these experiments are:

- **J. Kent Blaise, D. Pierce, Donatella Pascolini**, and A. **Scarpa** (University of Pennsylvania): "Time-Resolved Structural Studies of the Ca^{2+}-ATPase of Sarcoplasmic Reticulum Membranes Utilizing a Laser Plasma as a Source."
- **Leo Herbette** and **Robert McDaniel** (University of Connecticut): "Time-Resolved X-Ray Diffraction of Acetylcholine Receptor Membranes."

The one user experiment on the OMEGA system used six beams of 351-nm laser light focused onto spherical targets. The participating individuals of this experiment are:

- **Hans Griem** and **Samuel Goldsmith** (University of Maryland), **Uri Feldman** and **George Doschek** (Naval Research Laboratory), and **W. E. Behring** (Goddard Space Flight Center).

During the last fiscal year (1 October 1982 to 30 September 1983), the user program accumulated a total of 368 shots on both the GDL and the OMEGA facilities. These user experiments represented a broad range of scientific investigations. Table 17.2 shows the shot distribution for users during this period.

We are now in the process of soliciting proposals for the next NLUF Steering Committee meeting. This year, our committee will require submission of proposals by 1 April 1984. A revised description of the user facility and funding opportunities is included below.

User Experiments

User experiments are accessible at the University of Rochester for applications in high-energy-density physics. High-energy-density physics experiments use an intense pulse of laser light focused to a diameter of approximately 10^{-3} cm. Intensities of 10^{17} W/cm^2 can be created, equivalent to an electric field intensity of 10^9 V/cm. A solid material, irradiated by such an intense laser pulse rapidly becomes a plasma with temperatures of 10^7-10^8 K at densities of 1-10 g/cm^3. This point-source plasma thus provides the necessary conditions for studies of thermonuclear fusion, spectroscopy of highly ionized atoms, shockwaves, laboratory astrophysics, and the fundamental physics of matter under high intensities. Additional research opportunities are available for pulsed x-ray-diffraction experiments by using x rays emitted from a laser-produced plasma. This x-ray point source emits 10^{15} photons in 10^{-9} s at 4.4 Å (for a chlorine target). An x-ray collector can be used to deliver 10^{10} photons to a sample. The university facility has accommodated 30 user experiments since 1979.

Funds Available

The U.S. Department of Energy (DOE) has designated the Laboratory for Laser Energetics at the University of Rochester as a national facility, available to qualified researchers nationwide. DOE supports facility operation and provides research contracts for user experiments in laser fusion, plasma physics, and associated applications. Approximately *$720,000 of user research funds* will be available for the next period. User proposals in other areas can be accepted; however, funding support will have to be obtained separately through other agencies (e.g., the NSF). Proposals requesting allocation of facility time should be submitted to the NLUF Manager by *1 April 1984*. Proposal review is provided by the NLUF Steering Committee.

Facility

The 24-beam, 12-trillion-watt OMEGA laser system (at 1054 nm) provides the main high-power irradiaton capability of the Laboratory. The OMEGA system now has six beams converted to the ultraviolet

User System Shot Distribution
for Fiscal Year 1983
(1 October 1982 - 30 September 1983)

USER (Affiliation)	EXPERIMENT	NUMBER OF SHOTS
Frank Chen and Chan Joshi (UCLA), Nizar Ebrhaim (Yale University)	Plasma Instabilities	105
J. Kent Blasie and Leo Herbette (U. of Pennsylvania and U. of Connecticut)	Biophysics	77
Ray Elton and T. N. Lee (Naval Research Laboratory)	X-Ray Laser	25
Jim Forsyth and Robert Frankel (U. of Rochester)	Biophysics	107
Uri Feldman and George Doschek (Naval Research Laboratory)	VUV Spectroscopy	32
Hans Griem and Samuel Goldsmith (U. of Maryland)	Line Shifts	15
George Miley (U. of Illinois)	Particle Energy Loss	5
Barukh Yaakobi (U. of Rochester)	X-Ray Diagnostics	2*
*Plus other shots shared with other users.	TOTAL	368

SCHEDULED USER SHOTS

Burton Henke (U. of Hawaii)	X-Ray Diagnostics (1984)
Tom Blue (U. of Illinois)	Particle Measurements (1984)
C. F. Hooper, Jr. (U. of Florida)	Implosion Dynamics (1984)

U69

Table 17.2
User system shot distribution for fiscal year 1983 (1 October 1982-30 September 1983).

(351 nm). The six UV beams have a total energy of 300 J for 1-ns pulse widths. User experiments are possible with either UV or IR laser radiation. A single-beam replica of OMEGA, the Glass Development Laser (GDL, at 351 nm), is also available. The target areas at the NLUF allow users access to three separate chambers—one for OMEGA and two for GDL.

For more information about proposal guidelines and the resources available at the NLUF, please contact:

Thomas C. Bristow, Manager
National Laser Users Facility
Laboratory for Laser Energetics
University of Rochester
250 East River Road
Rochester, New York 14623
(716) 275-2074

ACKNOWLEDGMENT

This work was supported by the U.S. Department of Energy Office of Inertial Fusion under contract number DE-AC08-80DP40124.

PUBLICATIONS AND CONFERENCE PRESENTATIONS

Publications

G. J. Linford, B. C. Johnson, J. S. Hildum, W. E. Martin, K. Snyder, R. D. Boyd, W. L. Smith, C. L. Vercimak, D. Eimerl, J. T. Hunt, W. Seka, R. S. Craxton, S. D. Jacobs, L. D. Lund, R. L. McCrory, and J. M. Soures, "Large Aperture Harmonic Conversion Experiments at LLNL: Comments," *Appl. Optics* **22**, 1957-1958 (1983).

J. Delettrez, A. Entenberg, Y. Gazit, D. Shvarts, J. Virmont, T. Bristow, J. M. Soures, and A. Bennish, "Time Decay of Electric Fields Probed by Charged Reaction Products in Six Beam Symmetrical Implosion Experiments," *Nucl. Fusion* **23**, 1135-1141 (1983).

P. A. Jaanimagi and M. C. Richardson, "Streak Camera for Picosecond X-Ray Diagnostics," *Rev. Sci. Instrum.* **54**, 1095-1099 (1983).

J. A. Abate and R. Roides, "Spatially Resolved Absorption and Detection of Microscopic Impurities in Optical Thin Films by Photothermal Detection," *J. Phys. (Paris)* supplément au n°10, **44**, C6-497 (1983).

A. Simon, R. W. Short, E. A. Williams, and T. Dewandre, "On the Inhomogeneous Two-Plasmon Instability," *Phys. Fluids* **26**, 3107-3118 (1983).

B. Yaakobi, H. Kim, and J. M. Soures, "Submicron X-Ray Lithography Using Laser Produced Plasma as a Source," *Appl. Phys. Lett* **43**, 686-688 (1983).

B. Weinstein, T. Orlowski, W. Knox, T. Nordlund, and G. Mourou, "Picosecond Luminescence and Competing Nonradiative Process in As_2S_3 Glass," *Phys. Rev. B* **26**, 4777-4780 (1983).

S. A. Letzring, E. I. Thorsos, W. D. Friedman, W. Seka, and J. E. Rizzo, "An Absolutely Timed X-Ray Streak Camera for Laser Fusion Experiments," *J. Appl. Phys.* **54**, 6302-6306 (1983).

I. Lubezky and A. Lubezky, "Practical Design and Double Layer Anti-Reflective Coatings for High Index Substrates," *Opt. Engineer.* **22**, 753-755 (1983).

W. Knox and L. Forsley, "Data Acquisition System for A Jitter-Free Signal Averaging Streak Camera," ACS Symposium Series No. 236 Multichannel Image Detectors **2**, ACS, 1983.

Forthcoming Publications

S. Skupsky, R. L. McCrory, R. S. Craxton, J. Delettrez, R. Epstein, K. Lee, and C. Verdon, "Uniformity of Energy Deposition for Laser-Driven Fusion." *Laser Interaction and Related Plasma Phenomena*, edited by H. Hora and G. Miley (Plenum Press, New York, 1983, in press).

H. Kim, T. Powers, and J. Mason, "Inertial Fusion Target Fabrication Using Polystyrene Mandrels," accepted for publication by *Journal of Vacuum Science and Technology*.

W. Knox and L. Forsley, "Interactive Programming Applied to a Jitter-Free Signal Averaging Streak Camera," to be published in the *Proceedings on Multichannel Detectors* by the American Chemical Society.

B. Yaakobi, J. Delettrez, R. L. McCrory, R. Marjoribanks, M. C. Richardson, D. Shvarts, S. Skupsky, J. M. Soures, C. Verdon, D. Villeneuve, T. Boehly, R. Hutchison, and S. Letzring, "Thermal Transport Measurements in 1.05-μm-Laser Irradiation of Spherical Targets." accepted for publication by *Physics of Fluids*.

B. Yaakobi and A. Burek, "Crystal Diffraction Systems for X-Ray Spectroscopy Imaging and Interferometry of Laser Fusion Targets," accepted for publication by *IEEE Journal of Quantum Electronics*.

M. C. Richardson, R. Marjoribanks, S. Letzring, J. Forsyth, and D. Villeneuve, "Spectrally Discriminating Time-Resolved and Space-Resolved X-Ray Plasma Diagnostics," accepted for publication by *IEEE Journal of Quantum Electronics*.

N. S. Murthy and H. Kim, "Molecular Packing in Alkylated and Chlorinated Poly-p-paraxylylenes," accepted for publication by *Polymer*.

D. M. Villeneuve, R. Keck, B. Afeyan, W. Seka, and E. Williams, "Production of Hot Electrons by Two Plasmon Decay Instability in UV Laser Plasma," accepted for publication by *Physics of Fluids*.

M. C. Richardson, S. Skupsky, J. Kelly, L. Iwan, R. Hutchison, R. Peck, R. L. McCrory, and J. M. Soures, "Laser Fusion Target Irradiation Uniformity with the 24-Beam OMEGA Facility," accepted by *SPIE Vol. 380, Proceedings of 1983 Los Alamos Conference on Optics*.

M. C. Richardson, S. A. Letzring, W. Friedman, and G. Gregory, "Time-Resolved X-Ray Photography of Uniformly Irradiated Spherical Targets," accepted by *SPIE Vol. 427, Proceedings of High-Speed Photography, Videography, and Phototonics*, San Diego, CA, 1983.

Conference Presentations

L. P. Forsley, "Real Time Interactive Spectroscopy," presented at the National Forth Convention, Palo Alto, California, October 1983.

J. F. Whitaker and D. Smith, "Electrical Pulse Shaping Using Multiple Solid State Switches," presented at the IEEE Electron Device Conference at the Rochester Institute of Technology, Rochester, New York, October 1983.

R. L. McCrory, "Inertial Fusion Research at the University of Rochester: Progress in Direct Drive," presented at the International Atomic Energy Agency (IAEA) Technical Committee Meeting on Advances in Inertial Confinement Fusion, Kobe, Japan, November 1983.

J. Abate, A. Schmid, M. Guardalben, D. Smith, and S. Jacobs, "Characterization of Micron-Sized, Optical Coating Defects by Photothermal Deflection Microscopy," presented at the Fifteenth Annual Symposium on Optical Materials for High Power Lasers, Boulder, Colorado, November 1983.

The following presentations were made at the Annual Meeting of the Optical Society of America, New Orleans, Louisiana, October, 1983:

T. G. Dziura and D. G. Hall, "A Semiclassical Theory of Bistable Semiconductor Lasers."

R. Frankel and J. M. Forsyth, "Observation of Photostructural Activity in Bacteriorhodopsin Using a Laser Driven X-Ray Source."

S. D. Jacobs and K. A. Cerqua, "Liquid Crystal Laser Blocking Filter."

J. H. Kelly, "Beam Profile Control in the OMEGA Laser System."

L. D. Lund, "Active Mirror Nd:Glass Amplifiers" (invited).

The following presentations were made at the 1983 Nuclear Science Symposium, San Francisco, California, October 1983:

G. Mourou, J. Valdmanis, and S. Williamson, "New Approaches to Electrical Transient Sampling Systems with Picosecond Resolution" (invited).

G. Mourou, W. Knox, and S. Williamson, "Picosecond High Power Switching and Applications" (invited).

The following presentations were made at the Thirtieth National Symposium of the American Vacuum Society, Boston, Massachusetts, November 1983:

H. Kim, T. Powers, and J. Mason, "Inertial Fusion Target Fabrication Using Polystyrene."

B. Yaakobi, H. Kim, and J. M. Soures, "Sub-Micron X-Ray Lithography Using UV-Laser Produced Plasma as a Source."

The following presentations were made at the Twenty-Fifth Annual Meeting of the APS Division of Plasma Physics, Los Angeles, California, November 1983:

B. B. Afeyan, E. A. Williams, R. W. Short, and A. Simon, "Improvements to the Linear Theory of the Absolute S.R.S. Instability."

T. Boehly, L. M. Goldman, W. Seka, and R. S. Craxton, "Hydrodynamic Efficiency of Planar Targets Irradiated with 0.35-μm Laser Light."

R. S. Craxton and R. L. McCrory, "Thermal Self-Focusing in Laser-Plasmas with Self-Consistent Hydrodynamics."

J. Delettrez, R. S. Craxton, R. Epstein, O. Barnouin, M. C. Richardson, J. M. Soures, and B. Yaakobi, "Simulation of the Thermal Electron Transport Experiments in Spherical Irradiation at λ=0.35 μm."

R. Epstein, S. Skupsky, J. Delettrez, and B. Yaakobi, "Spectral Signatures of Non-Maxwellian and Non-LTE Effects in Thermal Transport Experiments."

R. L. Keck, M. C. Richardson, W. Seka, J. M. Soures, and R. Hutchison, "Absorption and Hot Electron Generation for UV Laser Spherically Irradiated Targets."

S. A. Letzring, M. C. Richardson, J. Delettrez, and G. Gregory, "Time-Resolved X-Ray Photography of Imploding Large Aspect Ratio Targets."

R. S. Marjoribanks, M. C. Richardson, J. Delettrez, and S. A. Letzring, "Time-Resolved X-Ray Spectrometry Studies of Transport in Symmetric Layered Targets."

C. McKinstrie and A. Simon, "Non-Linear Saturation of the Stimulated Raman Instability."

D. Quick, S. P. Saraff, S. A. Letzring, and M. C. Richardson, "Thermal (<10 keV/Z) and Non-Thermal (>10 keV/Z) Ion Measurements of 0.35-μm Laser Produced Plasmas."

M. C. Richardson, J. Delettrez, R. L. McCrory, W. Seka, S. Skupsky, J. M. Soures, C. P. Verdon, B. Yaakobi, S. A. Letzring, and R. L. Hutchison, "Short Wavelength Direct Drive Laser Fusion Experiments."

M. C. Richardson, P. L. Hagelstein, M. J. Eckart, J. M. Forsyth, M. Gerrassimenka, and J. M. Soures, "Photoionization X-Ray Laser Studies in Neon."

S. P. Sarraf, S. A. Letzring, and M. C. Richardson, "Thermal (<10 keV/Z) and Non-Thermal (>10 keV/Z) Ion Measurements of 0.35-μm Laser Produced Plasmas."

W. Seka, "Single Beam Interaction Experiments at 0.35-μm at the University of Rochester" (invited).

W. Seka, R. Boni, L. M. Goldman, M. C. Richardson, K. Tanaka, R. Short, J. M. Soures, and E. A. Williams, "Half-Integer Harmonic Radiation from Laser Plasmas."

R. W. Short and E. A. Williams, "Underdense Parametric Phenomena in Filaments."

S. Skupsky, J. Delettrez, and C. P. Verdon, "The Effect of Thermal Flux Saturation on Lateral Heat Transport-Multigroup Analysis."

J. M. Soures, M. Dunn, R. Hutchison, L. Iwan, W. Lampeter, L. D. Lund, D. Quick, M. C. Richardson, W. Seka, and S. Skupsky, "Irradiation Uniformity of Multi-Beam, Short-Wavelength, Direct-Drive Laser Facility."

M. Strauss, G. Hazak, D. Shvarts, and R. S. Craxton, "Magnetic-Field Effects on Electron Heat Transport in Laser-Produced Plasma Physics."

K. Swartz, E. A. Williams, and J. R. Albritton, "Heat Front Penetration by a Non-Maxwellian Electron Tail."

K. Tanaka, L. M. Goldman, M. C. Richardson, W. Seka, R. W. Short, J. M. Soures, and E. A. Williams, "Evidence of Parametric Instabilities in Second Harmonic Spectra from Laser (1μm) Produced Plasma."

E. A. Williams, "Stimulated Emission From Convectively Unstable Inhomogeneous Plasma."

B. Yaakobi, O. Barnouin, J. Delettrez, L. M. Goldman, R. L. McCrory, M. C. Richardson, and J. M. Soures, "Thermal Transport and Preheat Measurements in Spherical Irradiation at λ=0.35 μm."

The following presentations were made at the 1983 IEEE International Electron Devices Meeting, Washington, D.C., December 1983:

G. Mourou and J. Valdmanis, "Picosecond and Subpicosecond Electronics for Measurements of Future High-Speed Electronic Devices."

J. A. Valdmanis, G. Mourou, and C. W. Gabel, "Subpicosecond Electrical Sampling."

The following presentations were made at the Tenth Symposium on Fusion Engineering, Philadelphia, Pennsylvania, December 1983:

L. Lund, S. Skupsky, and L. M. Goldman, "Uniformity Analysis for a Direct Drive Laser Fusion Reactor."

J. M. Soures, R. J. Hutchison, S. D. Jacobs, L. D. Lund, R. L. McCrory, and M. C. Richardson, "OMEGA: A Short-Wavelength Laser for Fusion Experiments" (invited).

The work described in this volume includes current research at the Laboratory for Laser Energetics which is supported by Empire State Electric Energy Research Corporation, General Electric Company, New York State Energy Research and Development Authority, Northeast Utilities Service Company, The Standard Oil Company, University of Rochester, and the U.S. Department of Energy Office of Inertial Fusion under contract DE-AC08-80DP40124.